ABSTRACT

Impact of Microphysical Interactions on Aggregate Morphologies

Jonathan Perry, M.S.

Advisor: Lorin S. Matthews, Ph.D.

Coagulation of (sub)micron-sized dust particles occurs in a variety of environments; such as the interstellar medium, protoplanetary disks, Earth's upper atmosphere and industrial processes. Understanding the physics of collisions and interparticle interactions of dust grains within this size regime is essential to understanding such environments. To gain detailed insight into the parameters which enhance or inhibit coagulation it is beneficial to employ numerical methods to grow aggregates where the degrees of freedom may be tuned to a multitude of possible parameter sets. Two of the possible numerical methods which may be employed are pair-wise simulations or N-body simulations.

This work expands upon previous numerical methods by examination of the combined effects of electrostatic and magnetostatic interactions. Effects of these interactions, alone and in combination, are examined based upon collision probabilities as well as the resulting aggregate structures. Also examined are the variations induced by employing ellipsoidal monomers during aggregation.

Impact of Microphysical Interactions on Aggregate Morphologies

by

Jonathan Perry, B.A.

A Thesis

Approved by the Department of Physics

_____

Gregory A. Benesh, Ph.D., Chairperson

Submitted to the Graduate Faculty of
Baylor University in Partial Fulfillment of the
Requirements for the Degree
of
Master of Science

Approved by the Thesis Committee

_____

Lorin S. Matthews, Ph.D., Chairperson

_____

Manfred H. Dugas, Ph.D.

_____

Truell W. Hyde, Ph.D.

Accepted by the Graduate School
August 2012

_____

J. Larry Lyon, Ph.D., Dean

Page bearing signatures is kept on file in the Graduate School.

TABLE OF CONTENTS

LIST OF FIGURES vi

LIST OF TABLES xi

ACKNOWLEDGMENTS xii

1 Introduction 1

1.1 Astrophysical Coagulation 1

1.1.1 Protoplanetary Disks 1

1.1.2 Mesospheric Dust 4

1.1.3 Cometary Dust 6

1.2 Dusty Plasma 7

1.3 Interparticle Forces 9

1.3.1 Electrostatics 9

1.3.2 Magnetostatics 10

1.4 Monomer Shape 10

1.5 Thesis Progression 11

2 Dynamics and Interactions of Dust Grains 12

2.1 Relative Velocities 12

2.1.1 Brownian Motion 12

2.1.2 Vertical Settling 13

2.1.3 Radial Drift 14

2.1.4 Turbulence 15

2.2 Charging of Dust Grains 16

2.3 Electrostatic Interactions 19

2.4 Magnetostatic Interactions 20

2.5 Collisional Cross-section 21

3 Numerical Methods 24

3.1 Aggregate Builder 24

3.2 Box Tree 27

3.3 Numerical Charging of Aggregates 29

3.3.1 Charging Current Density 29

3.3.2 LOS Algorithm 30

3.3.3 OML Algorithm 33

3.3.4 Charging of Ellipsoidal Monomers 34

3.4 Approximation of Charge and Electric Dipole Moments on Aggregates 37

3.5 Physical Analysis 38

3.5.1 Porosity 39

3.5.2 Fractal Dimension 40

3.5.3 Compactness Factor 40

3.5.4 Friction Time 41

4 Electromagnetic Dipole Interactions 43

4.1 Pair-wise Interactions 43

4.1.1 Initial Conditions 43

4.2 Results 44

4.2.1 Charge and Dipole Moments 44

4.2.2 Collision Probability 45

4.2.3 Fractal Dimension 48

4.3 Magnetic Contribution to Pair-wise Aggregation 52

4.4 N-body Dipole-Dipole Interactions 53

4.4.1 Initial Conditions 53

4.4.2 *box_tree* Aggregation 53

4.5 Summary 59

5 Effect of Monomer Shape on Aggregate Morphology 61

5.1 Motivation 61

5.2 Aggregation of Non-Spherical Particles 62

5.2.1 Aggregate Morphologies 63

5.2.2 Implications 69

5.3 Polydisperse Monomer Populations 70

5.3.1 Analysis of Polydisperse Aggregation 71

5.3.2 Implications 79

5.4 Aggregation of Charged Ellipsoids 80

5.4.1 Charge Arrangement 80

5.4.2 Post-Coagulation Structure 82

6 Conclusions and Future Work 84

6.1 Electromagnetic Interactions 84

6.2 Non-Spherical Monomers 86

6.3 Future Work 87

BIBLIOGRAPHY 89

LIST OF FIGURES

1.1 Pictogram of the structure and spatial scales of a protoplanetary disk. Reproduced from Wurm et al. 2010 [9]. 2

1.2 Noctilucent cloud formation taken from 36,000 feet above the south of Nunivak Island, Alaska. Courtesy of the AIM project, NASA. . . . 5

1.3 Dust plasma in a GEC RF Reference cell, lit by an argon laser beam. Photo provided courtesy of CASPER, Baylor University. 8

3.1 Approximation of the surface of a spherical monomer using 420 area patches. 31

3.2 Charging currents to a monomer within an aggregates. The open lines of sight to points A, B, C, and D on a monomer are indicated by the shaded regions. 31

3.3 Geometry to determine if sample test direction from point B on the surface of a monomer k is blocked by another monomer j. 32

3.4 Basic scheme of OML_LOS. This image has been reproduced by permission of Ma [71]. 34

3.5 Open and blocked lines of sight (LOS) for a patch on an ellipsoidal monomers. Dashed lines represent blocked lines of sight while solid lines indicate open lines of sight, along which electrons and ions may impact the particle. 35

3.6 Arrangement of charges on a prolate ellipsoidal monomer. The bulk of the negative charges collect on the high curvature ends of the ellipsoid due to their larger LOS factors. This charge arrangement will also lead to a small dipole due to the separation of charges on the ends. 37

3.7 Charge ratio versus length/diameter ratio using monomers of constant volume. The charge is seen to increase as the length of the semi-major axis increases 38

3.8 An illustration of the compactness factor. The exterior shaded circle corresponds to the maximum radius of the aggregates, R_{max}, while the darker, inner shaded region corresponds to R_σ. For more compact structures, the ratio of the volumes approaches unity. For more open structures, the ratio of the volumes approaches zero. 41

4.1 Normalized cluster magnetic moment as a function of N, the number of monomers in an aggregate. The fit line shows an exponential increase $\mu \propto \mathrm{N}^{0.53}$. 45

4.2 Normalized magnetic moment of clusters as a function of N. The fit line shows an increase in dipole moment of $\mu \propto N^{0.68}$, greater that seen in Figure 4.1 for purely magnetic interactions. 46

4.3 a) Probability for collision of magnetic grains having an initial speed of $1/16 v_{th} \leq v \leq v_{th}$, b) Probability of collision for charged and charged-magnetic aggregates having an initial speed of $2v_{th} \leq v \leq 5v_{th}$. 47

4.4 Collision probability for charged, charged-magnetic, and neutral grains vs. impact parameter. 48

4.5 Comparison of aggregates formed from the following populations: a-b) Magnetic aggregates of $N = 22, F_d = 2.159$ and $N = 334, F_d = 1.789$ respectively. c-d) Charged aggregates with $N = 21, F_d = 2.333$, and $N = 595, F_d = 1.907$ respectively. e-f) Charged-magnetic aggregates of $N = 21, F_d = 2.359$, and $N = 504, F_d = 1.819$. g-h) Neutral aggregates with $N = 25, F_d = 2.403$ and, finally, $N = 589, F_d = 1.976$. 49

4.6 A comparison of the average fractal dimension for each population of aggregates as a function of size. Each line is a best fit to the fractal dimension of all aggregates with $N \geq 10$ in a given population. Error bars have been omitted for clarity. 50

4.7 Probability density estimates for the fractal dimensions of each population. a) Magnetic grains exhibit a local maximum at $F_d = 2.05$. b) charged aggregates have a broad distribution in fractal dimension. c) Charged-magnetic aggregates also show a broad distribution similar to charged aggregates, but have a larger percentage of aggregates with $F_d < 2.0$. d) Neutral aggregates have a relatively narrow peak at $F_d = 2.25$. 51

4.8 The number of aggregates within each population as the simulations progress. While the number of neutral aggregates decreases steadily over time, the populations which experience interparticle forces decrease in number more rapidly. 55

4.9 The size of the largest aggregates within each population as the simulation time moves forward. All populations are seen to have their largest aggregate grow slowly initially. Charged populations exhibit a very rapid accumulation of material upon the largest aggregate, termed run away growth. Magnetic and charged-magnetic populations appear to grow at a more sedate pace, though still more quickly than ballistic populations. 56

4.10 Electric dipole moment versus size. The fit lines for the two populations change according to $Q_q \propto I^{0.45}$ for charged aggregates and $Q_{\mu q} \propto I^{0.4762}$. 56

4.11 Normalilzed magnetic dipole moment versus size. The fit lines for the two populations change according to $\mu_\mu \propto N^{0.32}$ for magnetic aggregates and $\mu_{\mu q} \propto N^{0.42}$. 57

4.12 Average compactness factors versus size for all aggregate populations. 58

4.13 Evolution of average friction times versus size for all aggregate populations 59

5.1 Sample aggregates generated from the model described in the text a) PCA aggregate built from spheres (N = 20), b) CCA aggregate built from spheres (N $\sim$ 200), c) PCA aggregate built from spheres (N $\sim$ 700), d) PCA aggregate built from ellipsoids (N = 20), e) CCA aggregate built from ellipsoids (N $\sim$ 200), f) PCA aggregate built from ellipsoids (N $\sim$ 700). 63

5.2 Average porosities for a) populations built from CCA collisions, and b) populations built from PCA collisions. c) Percent difference between aggregates built using different monomer shapes within the same collision regime. The lines in a) and b) represent the porosities of populations grown without using an offset or rotation replicating the results of Bertini et al. [78]. The darker line corresponds to aggregates comprised of ellipsoidal monomers, while the lighter is for aggregates comprised of spherical monomers. In a) the differences between spheres and ellipsoids are so small that the trend lines coincide at all points. 65

5.3 Magnitude of rotations induced by off-center collisions during the aggregation process. Collisions between clusters are seen to produce much higher spin rates than collisions of a single particle with a cluster, as expected. 65

5.4 Average compactness factor (with associated errors) for a) populations built using CCA collisions, and b) populations built using PCA collisions. c) Percent difference between aggregates built using different monomer shapes in the same collision regime. 66

5.5 Average friction times (with associated errors) calculated using a normalized geometric cross-section and for arbitrary environmental parameters for a) populations built using CCA collisions, and b) populations built using PCA collisions. c) Percent different between aggregates built using different monomer shapes in the same collision regime. 67

5.6 Sample aggregates grown from populations using the method described in Section 2. Each aggregate contains ≈ 80 monomers using a-c) monodisperse spheres, prolate ellipsoids (3:1:1), and oblate ellipsoids (3:3:1), d) polydisperse spheres, e-g) polydisperse prolate ellipsoids with axis ratios (3:1:1), (5:1:1), and (10:1:1) respectively, and h-j) polydisperse oblate ellipsoids with axis ratios (3:3:1), (5:5:1), and (10:10:1) respectively. 72

5.7 Average R_σ versus mass built from the larger monodisperse population and two different polydisperse populations. The solid line shows the trend for the combined populations for each monomer shape with the slope, β, indicated for a) two types of ellipsoids with aspect ratios of $(3:1)$, compared to spheres, b) ellipsoids with aspect rations of $(5:1)$, and c) ellipsoids with aspect ratios of $(10:1)$. For clarity oblate and spherical populations have been offset by x10 and x100 respectively. 73

5.8 Average compactness factors versus normalized mass for aggregates built from the larger monodisperse population and two different polydisperse populations for a) spherical monomers, b-d) ellipsoidal prolate monomers with aspect ratios of $(3:1:1), (5:1:1)$, and $(10:1:1)$ respectively, and e-g) ellipsoidal oblate monomers with aspect ratios of $(3:3:1), (5:5:1)$, and $(10:10:1)$ respectively. . . 74

5.9 Average compactness factors versus number of monomers for second and third generation aggregates for a) spherical monomers, b-d) ellipsoidal prolate monomers with aspect ratios of $(3:1:1), (5:1:1)$, and $(10:1:1)$ respectively, and e-g) ellipsoidal oblate monomers with aspect ratios of $(3:3:1), (5:5:1)$, and $(10:10:1)$ respectively. 75

5.10 Standard deviations scaled by the average compactness factor versus scaled masses for a) monodisperse populations, b) polydisperse populations with $\alpha = 1.8$, and c) polydisperse populations with $\alpha = 3.5$. For the prolate and oblate populations, the black markers correspond to aspect ratios of $3:1$, the medium gray corresponds to aspect ratios of $5:1$, while the lightest gray denotes aspect ratios of $10:1$. 77

5.11 Normalized friction times versus normalized mass for aggregates built from the larger monodisperse population and two different polydisperse populations for a) spherical monomers, b-d) ellipsoidal prolate monomers with aspect ratios of $(3:1:1), (5:1:1)$, and $(10:1:1)$ respectively, and e-g) ellipsoidal oblate monomers with aspect ratios of $(3:3:1), (5:5:1)$, and $(10:10:1)$ respectively. 78

5.12 Standard deviations scaled by the average friction time versus normalized mass for a) monodisperse populations, b) polydisperse populations with $\alpha = 1.8$, and c) polydisperse populations with $\alpha = 3.5$. For the prolate and oblate populations, the black markers correspond to aspect ratios of $3:1$, the medium gray to aspect ratios of $5:1$, while the lightest gray denotes aspect ratios of $10:1$. 79

5.13 Charge mapping of aggregates built from a) $N = 48$ spherical monomers and b) $N = 64$ prolate ellipsoidal monomers. Colors correspond to the charge on each monomer in units of elementary charge. 81

5.14 Normalized charge of aggregates constructed from ellipsoidal monomers versus size. 82

5.15 The compactness factors of charged aggregates composed of charged particles (ellipsoids or spheres) versus size (N). 83

LIST OF TABLES

5.1 Aspect ratio and sizes for monomer shapes used to grow aggregates through ballistic collisions. Min/max sizes for each monomer shape correspond to equal volumes. 71

ACKNOWLEDGMENTS

I would like to extend my acknowledgments to anyone who beneficially interacted with this work these past few years. This material is based upon work supported by the National Science Foundation under Grant No. 0847127.

CHAPTER ONE

Introduction

The process by which dust particles collide, stick together and grow to larger sizes is called coagulation. This process may occur in environments where densities and temperatures are high enough that the probability of a collision on short times scales, compared to the life of the environment itself, are high. Coagulation for (sub)micron-sized particles has been recognized as an area of importance in a variety of areas. Physical systems where coagulation can occur on Earth include atmospheric pollution [1], industrial milling processes [2, 3], and the growth of aerosols in the atmosphere [4]. Beyond Earth's atmosphere coagulation can occur in dense regions of molecular gas clouds [5], during the collapse of molecular cloud cores [6] and within protoplanetary disks leading to planet formation [7].

1.1 Astrophysical Coagulation

1.1.1 Protoplanetary Disks

Formation of solar systems, along with the planets, comets, and asteroids contained within them, are believed to form as a result of collapsing galactic nebulae, which themselves contain all the materials necessary for stellar and rocky body formation. As a nebula contracts, the densest, hottest region of gas will eventually ignite a fusion cycle, forming a protostar. Surrounding the protostar will be a mass of the remaining nebular material, which as it contracts will experience an increased rotation, via the conservation angular momentum, and flatten out into a disk of gas and dusty material which is termed a protoplanetary disk (PPD). Recent spectral observations (analyzing energy distributions) and direct imaging definitively show a number of young stars to be surrounded by PPD's [8], indicating that planet

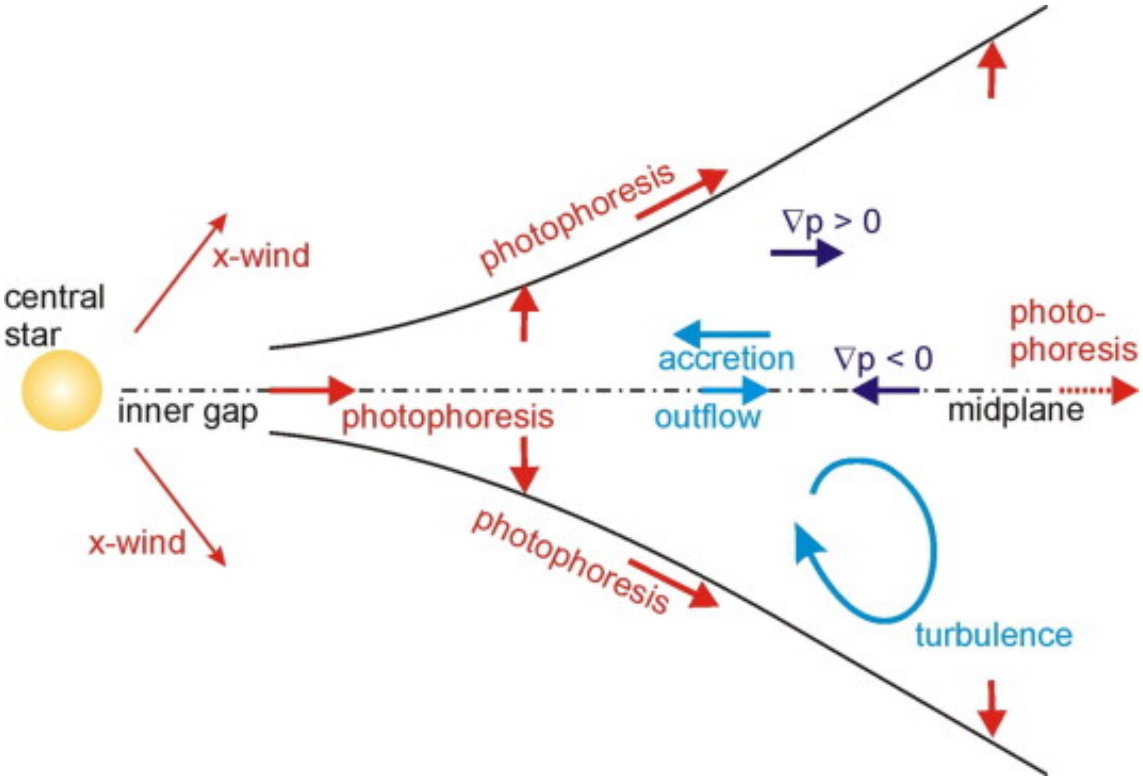

Figure 1.1: Pictogram of the structure and spatial scales of a protoplanetary disk. Reproduced from Wurm et al. 2010 [9].

formation is a common occurrence. Initially, these PPD's are vast, spanning radially outward from the protostar to several hundred astronomical units (AU, the average distance between the Earth and the sun) [10]. While the life time of protoplanetary disks far exceeds that of any observer (as well as the whole span of human existence), observations suggest that some PPD's have lifetimes up to around 10 million years [11].

Planets, and other solar bodies, are formed from this disk [12]. A sketch of the basic structure of a PPD from a recent review on planet formation is shown in Figure 1.1 [13]. Near a protostar a PPD is relatively thin, with a high dust and gas density. Further away from the protostar the PPD flares, increasing its thickness and becoming less dense.

One of the first stages in the growth of large bodies, such as planets, is the collision or coagulation of (sub)micrometer-sized dust particles. At such small sizes the dust particles are well embedded in the gaseous disk, which means that the motion of the dust is almost completely determined by the motion of the gas itself. In order to coagulate, dust grains must either have random motions superimposed on the mean gas motion or experience some force(s) which act to draw them together. Early work on small solid bodies in solar nebula concluded that all dust grains, regardless of size and their relative coupling to the gas motion, possess a velocity relative to the gas. These velocities may be induced by thermal (Brownian) motion, systematic motion due to vertical settling, orbital motion of the gas or by gas turbulence [14]. Any of these mechanisms will induce random motion by the dust particles thereby increasing the likelihood of collisions.

Another method by which collisions can occur in PPD's is through the influence of interparticle forces. Of the four fundamental forces, only gravity and electromagnetism act macroscopically, that is to say, on the classical scale. For (sub)micron-sized particles the mutual acceleration due to gravity is so small ($a < 10^{-12} \frac{m}{s^2}$), that it may be neglected as an influence on the local motion of the dust particles. This leaves electromagnetism as the only candidate for an interparticle force which may induce collisions in such environments.

Some materials within a PPD may have an intrinsic magnetic moment, either due to the material properties (such as ferromagnetic grains), or from environmental effects such as lightning discharges within the nebula [15]. So long as the dust temperature is below the Curie point for the material, this magnetism will be locked in, creating a magnetic dipole in dust grains which will interact with other magnetic materials nearby.

Collision and coagulation of dust grains within PPD's have been studied both experimentally and numerically [16, 17, 18, 19]. A majority of these models tend to focus specifically on ballistic aggregation (no interparticle forces) of spherical monomers. Additional models have examined electrostatic and magnetostatic interactions separately under different environmental parameters [20, 21]. Two important factors are neglected in previous literature: examination of electro- and magnetostatic forces in combination under the same environmental parameters and the effect of non-spherical monomers on the morphology and evolution of dust populations. Dust grains have the potential to become charged and/or be ferromagnetic in optically thin regions of the inner PPD. Though environmental parameters of molecular clouds and PPD's are uncertain, grains which are exposed to the primordial solar wind and UV radiation may become charged. Grains which are exposed to sufficiently strong UV radiation can acquire positive charges.

These grains, which will tend to a negative charge, have been shown to retard coagulation rates. Dust grains which become charged to the same potentials experience severely reduced coagulation rates [22]. Dust particles which experience different charging rates can also lead to oppositely charged grains within a single population of dust. If dipole-dipole electrostatic interactions are considered, the coagulation rate will be enhanced as dipolar forces are attractive [23]. The result of the charging and magnetization of dust grains will result in force interactions due to the electric and magnetic fields generated by each particle.

1.1.2 Mesospheric Dust

The mesosphere is an atmospheric layer located between 70-100 km above Earth's surface. Due to a combination of a lack of solar heating and strong radiative cooling from CO_2, the boundary between the mesosphere and the thermosphere is the coldest place on Earth. The lowest temperatures at this boundary, termed the

Figure 1.2: Noctilucent cloud formation taken from 36,000 feet above the south of Nunivak Island, Alaska. Courtesy of the AIM project, NASA.

mesopause, varies between 110K in the summer and 190 K or more in the winter [24, 25]. This variation in temperature is referred to as the mesopause anomaly.

The low temperatures in the summer mesopause leads to the condensation of atmospheric gases, including water. Water ice crystals then form a pervasive polar cloud layer termed polar mesospheric clouds, or noctilucent clouds (NCL's), as portrayal of which is seen in Figure 1.2 [26]. Concurrent with the formation of NCL's, strong radar echoes are observed, which, to date, have been unable to be explained either by scattering theory or disturbances induced by turbulence [27, 28, 29]. NCL's are investigated as a means of studying atmospheric conditions on both short (minutes) and long (decades) time scales using a variety of methods [30, 31]. These cloud formations are known to strongly influence their environment through trace gas redistribution. Understanding the formation of such cloud structures is a major step in quantifying their influence on atmsopheric processes.

Every day, the Earth's atmosphere encounters tons of meteoric material, most of which is ablated by heat and friction at altitudes ranging between 70 and 100 km [32]. This ablated material, termed meteoric smoke particles, has been conjectured to play an important role in atmospheric processes, such as the nucleation of ice particles and in polar summer mesospheric echoes (PSME) [33]. It is useful, therefore, to investigate the way meteoric smoke particle coagulate with each other and icy particles in the mesosphere, leading to the formation of NCL's.

It has been proposed that charged dust in the mesopause may account for the presence of PMSEs [34]. Due to their small size ($r < 0.1$) and surface impurities, meteoric dust particles may achieve high surface potentials when exposed to strong solar radiation. The charging process of dust grains follows from the ion and electron currents incident on the grain surface. Once charged, dust grain motions will be altered by interparticle forces via electrostatic interactions.

1.1.3 Cometary Dust

Comets are formed from the same initial materials as are planets, forming through the aggregation of small particles and growing up to the size of small bodies seen in the solar system today. When a comet passes close to the sun and is exposed to high amounts of solar radiation, individual aggregates may be lifted from the surface, forming a dust coma surrounding the main body [35]. These particles, which are initially a mixture of carbonaceous material and ices, will undergo evaporation, leaving only the small carbonaceous particles within the aggregates.

Cometary dust comae are studied via the observed strength of emission spectra of specific comets as a way of quantifying the behavior and structure of the aggregates lifted by solar radiation [36]. Cometary aggregates are believed to be highly porous structures, containing lots of open space within the extended strucutre. Various size distributions of the constituent dust particles have been put forth by different studies

in the past decades [37, 38]. Knowing the structure of cometary aggregates can give insight into the composition of the comets themselves as well as the environment in which they formed.

1.2 Dusty Plasma

Dust immersed in environments described in Section 1.1 have the potential to become charged when the surrounding gas is a plasma. To become a plasma the gas in the environment must be ionized, a process involving the removal of electrons from the outer electron orbits of atoms, which is a function of temperature, density and incident energy (such as from UV radiation). Optically thin regions of PPDs, planetary ring systems and cometary dust may have sufficient photon densities necessary to ionize the gases present. The mesosphere can receive a comparatively large flux of strong ultraviolet radiation especially during the summer months. The ionization of gas particles introduces two distinct species, ions and electrons. Figure 1.3 is an exhibition of an artificial dusty plasma in a GEC RF Reference Cell, illuminated by an argon laser beam.

Within a plasma, ions are typically assumed to have low mobility compared to electrons due to their high mass, and the faster moving electrons tend to accumulate preferentially on the surface of dust particles, charging them negatively. The number of electron charges on dust grains can be as small as an electron or two for nanometer sized grains up to several thousand electron charges for micrometer sized grains. Dust may also be charged by other methods, such as secondary electron emission, thermionic emission, or triboelectric charging [39].

When dust is exposed to strong fluxes of ultraviolet radiation or X-rays, some electrons may acquire sufficient energy to be emitted from the dust surface. The outward flux of photoelectrons represents a positive current which, when dominant over local negative currents, permits the dust grain to acquire a positive charge.

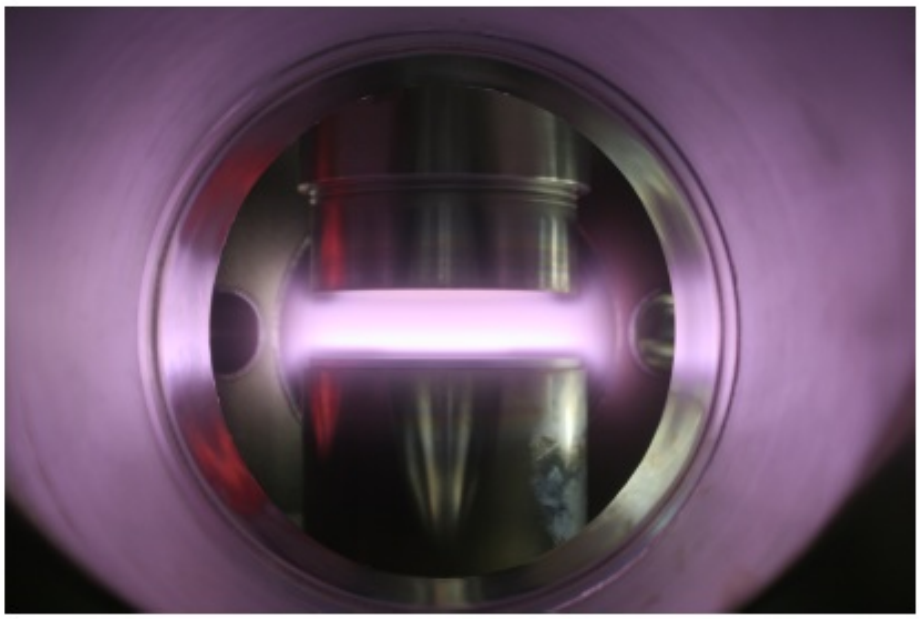

Figure 1.3: Dust plasma in a GEC RF Reference cell, lit by an argon laser beam. Photo provided courtesy of CASPER, Baylor University.

Secondary electron emission can occur when high energy electrons or ions are incident on the dust surface. High-energy electrons or ions are able to penetrate the dust particle surfaces and excite molecular electrons via scattering, which then escape as secondaries, contributing to the positive current around the grain. Thermionic emission is a process where electrons are emitted from the surface of dust particles when the local thermal energy available is large enough to overcome the binding potential energy, or work function of the material. As the surface temperature of the particle increases the flux of emitted thermal electrons also increases. Field emission is the ejection of electrons as induced by external electromagnetic fields. For small dust grains, field emission of electrons limits the magnitude of the potential when it is less than zero.

When charged dust particles are present in a plasma, the dynamic equilibrium may differ significantly than when charged dust particles are absent. Dust grains provide a point for the recombination of electrons and ions, and they will also ex-

change momentum with the plasma particles via these collisions. Grains may also collide with other grains and coagulate into larger aggregates.

1.3 Interparticle Forces

1.3.1 Electrostatics

Dust immersed in a radiative environment, as described in the previous section, which becomes charged will interact electrostatically with other charged particles in their vicinity. To first order, treating each charged grain as a point particle, if all grains have a negative charge, then particles will experience electrostatic repulsion, as determined by Coulomb's Law, thereby lowering their probability of coagulating [40].

Grains which overcome this repulsion, through high initial velocities, will coagulate into an aggregate, a structure with more than one monomer, and the charges will rearrange themselves over the new surface of the combined particle. The charge distribution on the surface of aggregates can be represented by a multipole expansion of the surface potential. Aggregates comprised of charged monomers will have an electrostatic dipole, a quantity determined by the number of charges on the surface and their separations. Electrostatic dipole interactions will exert an additional attractive force between two grains, counteracting part of the Coulomb repulsion, raising the probability of collisions.

The overall strength of the electric charges and dipoles on aggregates, as well as the relative velocities between particles will determine the outcome of a potential collision encounter: hit or miss. In addition to this, electrostatic interactions also induce rotations of two approaching grains, due to the torques, which will alter the structure of the resulting aggregates.

1.3.2 Magnetostatics

Dust grains comprised of ferromagnetic materials, such as iron, may become magnetized through alignment with a nascent magnetic field emanating from the protostar, lightning discharges in the disk, or other currently unknown phenomena [41]. The presence of magnetized dust grains introduces an additional attractive force which draws grains together, increasing the rate of coagulation. It has been shown that, when neglecting electrostatic interactions, nanometer sized dust grains which have a magnetic dipole undergo rapid growth via dipolar alignment [21, 42].

Once a dust grain achieves magnetization, the only way it may lose it is if the atoms within the material are able to break their alignment. The most probable way for this to occur is if the surrounding gas becomes heated to a point where the dust temperature exceeds the Curie temperature. Examination of the simple model employed by Chiang and Goldreich [43] to determine the temperature profile of PPDs show that the dust temperature will remain below the Curie temperature (1043 K for iron) for $r > 0.2AU$, valid for modeling regions of a PPD important for planetary growth.

1.4 Monomer Shape

In the absence of the interparticle forces, described in Section 1.4, coagulation may still occur where grain coagulation is driven by random or thermal motions. Many numerical models have been employed to examine the dynamics and properties of such coagulation [44, 45, 46]. Almost all numerical models make an assumption of spherical monomers as the building blocks of aggregates.

There is some observational evidence, however, which indicates that dust present in astrophysical environments deviates from the simple symmetric spherical structure. Polarization of sunlight scattered by cometary dust suggests ellipsoidal dust grains, specifically with a major axis three times longer than the minor axes

[36]. Additional evidence for non-spherical particles has been observed within the mesosphere. Measurements of these particles has been the focus of ongoing research for many years, in order to determine the role that meteoric smoke particles play in the upper atmosphere. By employing optical analysis (considering aspheric particles) of recent ground based LIDAR measurements of meteoric smoke particles, it has been found that the aspect ratio of these particles may vary from 0.1 to 10 [47].

1.5 Thesis Progression

The goal of this work is to examine coagulation of dust, using 1) combinations of magnetostatic and electrostatic forces and 2) non-spherical monomers, focusing on prolate ellipsoids (which have one semi-major axis and two equal semi-minor axes, like a grain of rice) as well as oblate ellipsoids (which have two equal semi-major axes and one semi-minor axis, like an M&M). Aggregate populations will be examined via their morphologies based on the parameters of physically relevant environments.

Chapter 2 presents the fundamental parameters and interactions of charged and/or magnetized dust grains in plasma systems, as well as the mechanisms by which grains may become magnetized. Chapter 3 discusses the numerical methods employed to investigate the variation in dust coagulation due to the parameters previously described. Chapter 4 will present the results of studying electromagnetic interactions between dust grains. In Chapter 5, variations due to non-spherical grain shapes will be investigated and presented. Chapter 6 summarizes the implications of these results and discusses future efforts.

CHAPTER TWO

Dynamics and Interactions of Dust Grains

Coagulation of dust within various environments has developed into a broad and complex field where the growth of dust particles may lead to very different structures depending upon both the environmental parameters and the dust properties themselves. Dust particles, which may or may not be spherical in nature, immersed in a radiative environment may become charged, and, perhaps, become magnetized as well. These interactions will then lead to differing aggregation behaviors. This chapter is devoted to the description of the underlying physics which govern the dynamics and interactions of dust grains.

Introduction to the physics governing these processes begins with the driving processes behind relative motions between dust grains (Section 2.1). Next, the electrostatic interactions of dust grains and the charging process they undergo are discussed (Sections 2.2 & 2.3). The methods by which dust can become magnetized are then presented (Section 2.4). Lastly, the interaction cross-section of dust particles is derived and examined for various conditions (Section 2.5).

2.1 Relative Velocities

2.1.1 Brownian Motion

Particles which are suspended in a fluid (liquid, gas or plasma) are seen to posses a random drift velocity. This velocity is due to the transfer of momentum during collisions between the fluid constituents and the dust particles. As a fluid is heated, its constituents increase their average kinetic velocity, leading to larger transfers of momentum to particles immersed in the fluid, and thus higher velocities. This behavior, termed Brownian motion, after 19^{th} century botanist Robert Brown,

falls under the umbrella of Kinetic Theory, which is applicable to dusty environments, as the number density of dust particles is far smaller than the number density of plasma species.

The random drift velocity is determined by

$$v = \sqrt{\frac{k_b T}{m}} \tag{2.1}$$

where T is the gas or plasma temperature, m is the mass of the particle, and k_b is the Boltzmann constant. Typical velocities for dust particles, assuming particles of size ($r = 0.1 - 10\ \mu m$), with a temperature of 100 K, are on the order of $v \approx 10^{-2} - 10^{-1} m/s$. Particle trajectories within an environment are random. Monomers and aggregates of different sizes tend to have higher relative velocities. The Brownian relative velocity between two different sized dust grains is given by

$$v = \sqrt{\frac{8kT(m_1 + m_2)}{\pi m_1 m_2}} \tag{2.2}$$

using temperatures and masses consistent for nebular clouds or protoplanetary disks, it may be seen that the average relative velocity will always result in a sticking collision [5].

2.1.2 Vertical Settling

Dust particles distributed throughout a PPD, portrayed in Figure 1.1, extend radially out from the protostar are also suspended above and below the mid-plane of the disk. Consider a small particle immersed in a laminar disk, initially suspended some distance z above the mid-plane. The force acting on such a particle is

$$|F_{grav}| = m\Omega^2 z \tag{2.3}$$

where $\Omega = \sqrt{GM_*/r^3}$ is the local Keplerian angular velocity, m is the mass of the particle, and z is the height above or below the mid-plane of a disk. While the gas

in a disk is supported by an upward pressure gradient, no such force suspends solid particles. Assuming a particle starts from rest and accelerates downward from this gravitational force, in the Epstein drag regime the equation of motion becomes

$$|F_D| = \frac{4\pi}{3}\rho r^2 v_{th} v \tag{2.4}$$

where r is the radius of the particle, ρ is the gas density, and v_{th} is the sound speed. To determine the speed at which a dust particle settles, the previous equation may be solved for v

$$v_{settle} = \frac{\rho_m}{\rho}\frac{r}{v_{th}}\Omega^2 z \tag{2.5}$$

Typical speeds for dust particles approximately 1 AU above the mid-plane are $v_{settle} \approx 5 \times 10^{-4}\ m/s$. Generally this is a few orders of magnitude smaller than thermal or turbulent motions [48].

2.1.3 Radial Drift

Particle motion directed radially inward, towards the protostar, is induced by a combination of the drift of individual particles, v_d, and drift caused by the accretion process of the gas environment, v_{da}. The total radial drift velocity is then a combination of these two components: $v_D = v_d + v_{da}$. The radial drift speed fo individual dust particles of a certain mass m is given by [49]

$$v_d = -\frac{2v_N}{\tau_f \Omega + \frac{1}{\tau_f \Omega}} \tag{2.6}$$

where τ_f is the friction time, Ω is the orbital frequency, and v_N is the maximum radial drift velocity [50].

The gas contribution to the radial velocity, produced by the accretion of gas, is calculated via [51]

$$v_{da} = \frac{v_{gas}}{1 + \tau_f^2 \Omega^2} \tag{2.7}$$

where v_{gas} is the accretion velocity of the gas [52].

Relative velocities between particles due to radial drift is then simply the difference between the radial velocities of particles i and j. For astrophysically relevant environments the product $\tau_f \Omega$ is always smaller than 10^{-3}, so the gas accretion term may be safely neglected [53]. Thus the relative velocities between any two particles due to radial drift is

$$\Delta v_D = |v_{D,i} - v_{D,j}| \approx |v_{d,i} - v_{d,j}| \tag{2.8}$$

Assuming typical dust grains composed of silicate material with sizes on the order of $1 \rightarrow 10 \mu m$ and $\tau_f \Omega \approx 5 \times 10^{-3}$, the relative velocities between particles is on the order of $\Delta v_D \approx 1 \times 10^{-2}\ m/s$.

2.1.4 Turbulence

Within PPD's, there is a rather paradoxical event, where angular momentum is transferred radially outward while concurrently mass is transferred inward (radial drift). A explanation to this paradox has been proposed by the $\alpha - model$, where turbulent viscosity provides for the transfer of momentum via viscosity [54]. Within the model α is a free parameter between zero (for no accretion) and unity. This parameter is used to determine the viscosity by

$$\nu = \alpha c_g H \tag{2.9}$$

where c_g is the isothermal sound speed within the disk, and H is the gas scale height. At the time of this proposal in the 1970's, no mechanism was identified to provide for turbulent motion. Two decades later, a now popular theory was proposed, which linked magnetic instability with the turbulent motion arising in accretion disks [55].

Particles in the micrometer and submicronmeter size range, are the smallest particles to be found in PPD's and are thus strongly coupled to their gas environment and turbulent eddies. Relative velocities due to turbulence have been derived by Ormel and Cuzzi [56] and are given by the relation

$$\Delta V_{12} = \sqrt{\frac{3}{2}}\frac{V_\eta}{\tau_\eta}(\tau_1 - \tau_2) \tag{2.10}$$

where V_η and τ_η are the velocity and time scales of the smallest eddy, respectively, and τ_1 and τ_2 are the friction times of the two particles being considered. The turnover velocity and time scale, V_η and τ_η, are related to the velocity, length, and time scales of the largest eddies through the Reynolds number of the turbulent flow: $V_\eta \propto L_\eta/\tau_\eta, L_\eta = Re^{-3/4}L_L$ and $\tau_\eta = \tau_L Re^{-1/2}$.

The velocity, length and time scales of the largest eddies are given by Cuzzi et al. [57]

$$V_L = \sqrt{\alpha}c_g \tag{2.11}$$

$$L_L = \sqrt{\alpha}H \tag{2.12}$$

$$\tau_L = \Omega_K^{-1} \tag{2.13}$$

where, as before, c_g is the isothermal sound velocity, and H is the gas scale height. With these definitions the Reynolds number is defined as $Re = V_L L_L/v_m$, where v_m is the molecular viscosity of the gas, and $Re = \alpha c_g H/v_m$, where α corresponds to the $\alpha - model$ mentioned previously [54]. Relative velocities between two grains at 1 AU are in the range of $\Delta v \approx 0.1 \rightarrow 1.0 m/s$.

2.2 Charging of Dust Grains

Particles which are immersed in a plasma or radiative environment will become charged due to the incident currents from electrons and ions. When particles in proximity to one another are both charged they will experience interparticle electrostatic

forces due to the electric fields from the other particle. A simple assumption for such radiative environments is equal number densities of electrons and ions, $n_e = n_i = n_0$, and that the electron and ion temperatures are also equal, $T_e = T_i$. Under these conditions it is easy to see that electron current to the grain will initially be the dominant charging current, since ions are much more massive than electrons and thus have smaller thermal velocities. This leads to grains acquiring a negative equilibrium charge.

A generally used quantitative approach to the estimation of charge on dust grains immersed in a gaseous plasma is Orbital Motion Limited (OML) theory. This approach is based on the assumptions of conservation of energy and the conservation of angular momentum of incident electrons and ions to determine the cross-section for electron and ion collection on dust grains [58].

Conservation of angular momentum requires that the angular momentum at infinity is equal to that at the point of impact with the grain

$$m_{e,i} v_{e,i-s} s = m_{e,i} v_{e,i-\infty} b_{max} \tag{2.14}$$

where $m_{e,i}$ is the electron (ion) mass, s is the radius of the grain, b_{max} is the impact parameter, v_s is the electron (ion) velocity at the point of impact, and v_∞ is the electron (ion) velocity far away from the grain, essentially at infinity.

By the conservation of energy, the velocities of the electrons and ions at the surface of the grain and at infinity are related by

$$\frac{1}{2} m_{e,i} v_{e,i-s}^2 + q_{e,i}\phi_s = \frac{1}{2} m_{e,i} v_{e,i-\infty}^2 + q_{e,i}\phi_\infty \tag{2.15}$$

where $q_{e,i}$ is the charge of the electrons (ions), ϕ_s is the electrostatic potential at the surface of the grain and ϕ_∞ is the electrostatic potential far away from the grain. Using infinity as the reference point, such that $q_{e,i}\phi_\infty = 0$, then Equation 2.10 may be rewritten as

$$\frac{1}{2}m_{e,i}v_{e,i-s}^2 + q_{e,i}\phi_s = \frac{1}{2}m_{e,i}v_{e,i-\infty}^2 \tag{2.16}$$

Be combining Equations 2.9 and 2.11 the maximum impact parameter is given by

$$b_{max} = s\sqrt{1 - \frac{2q_{e,i}\phi_s}{m_{e,i}v_{e,i-s}^2}} \tag{2.17}$$

and the cross-section may be determined from $\sigma = \int_0^{b}{}_{max} 2\pi b db$. The cross-sections for electron and ion collection are then

$$\sigma = \begin{cases} \pi a^2(1 - \frac{2q_{e,i}\phi_s}{m_{e,i}v_\infty^2}), & \frac{2q_{e,i}\phi_s}{m_{e,i}v_\infty^2} < 1. \\ 0, & \frac{2q_{e,i}\phi_s}{m_{e,i}v_\infty^2} > 1. \end{cases} \tag{2.18}$$

It is clear that the cross-section for electrons and ions depends both on the polarity of the surface potential, as well as the velocity at infinity. Given the cross-section, the electron and ion currents incident on the grain may be calculated for a given velocity distribution, $f_{e,i}(v)$, by integrating [39]

$$J_{e,i} = \int q_{e,i}\vec{v_{e,i}}\sigma_{e,i}(\vec{v_{e,i}})f(\vec{v_{e,i}})d^3\vec{v_{e,i}} \tag{2.19}$$

With the assumption of spherical symmetry for the dust grains, the angular and radial components of $d^3\vec{v_{e,i}}$ may be separated [58]

$$d^3\vec{v_{e,i}} = v^2 dv d\Omega = v^2 dv sin\theta d\theta d\phi \tag{2.20}$$

Electrons and ions are typically assumed to have a Maxwellian distribution, given by

$$f(\vec{v_{e,i}}) = n_{e,i}(\frac{m_{e,i}}{2\pi kT_{e,i}})^{3/2} exp(-\frac{m_{e,i}v_{e,i}}{2kT_{e,i}}) \tag{2.21}$$

Using this distribution, the integration of Equation 2.17 yields electron and ion currents of the form

$$I_{e,i} = \begin{cases} \sqrt{8\pi}a^2 n_{e,i} q_{e,i} \sqrt{\frac{kT_{e,i}}{m_{e,i}}} exp(-\frac{q_{e,i}\phi_s}{kT_{e,i}}), & q_{e,i}\phi_s > 0. \\ \sqrt{8\pi}a^2 n_{e,i} q_{e,i} \sqrt{\frac{kT_{e,i}}{m_{e,i}}} (1 - \frac{q_{e,i}\phi_s}{kT_{e,i}}), & q_{e,i}\phi_s < 0. \end{cases} \tag{2.22}$$

Since $m_e \ll m_i$, dust grains immersed in plasma are negatively charged.

Though OML theory may be used to analytically compute the charging currents for simple shapes or numerically simulate the charging process for arbitrary shapes, the theory does have some limitations. First, the theory must satisfy [59]

$$a \ll \lambda_D \ll l_{e,i} \tag{2.23}$$

where λ_D is the plasma Debye length, and $l_{e,i}$ is the collisional mean free path of the electrons or ions. The first part of the condition, $a \ll \lambda_D$, ensures that the problem remains linear. The second part, $\lambda_D \ll l_{e,i}$, allows the mutual collisions between electrons and ions to be neglected.

2.3 Electrostatic Interactions

Once charged, dust grains will interact electrostatically. To first order this interaction will follow the well known Coulomb repulsion. Complete consideration of the electrostatic interactions must be expanded to include the dipole terms, in addition to monopole interactions, as dipolar attraction has been shown to enhance the coagulation rate of dust grains in previous studies [20]. The force acting on particle i due to the electrostatic forces of particle j are given by

$$\vec{F}_{i,j-e} = q_i \vec{E}_j \tag{2.24}$$

$$\vec{F}_{i,j-e} = (\vec{p_i} \cdot \nabla)\vec{E}_j \tag{2.25}$$

where $\vec{E}$ is the electric field, q is the charge, and $\vec{p}$ is the electric dipole. The force interactions will also induce a torque on each particle, causing it to rotate as the particles approach (or recede). The electric torque, $\vec{\tau}$, is calculated using

$$\vec{\tau}_{i,j} = \vec{p_i} \times \vec{E_j} \tag{2.26}$$

2.4 Magnetostatic Interactions

Particles which are magnetized act on each other via dipolar force interactions given by

$$F_{i,j-m} = (\vec{\mu_j} \cdot \nabla)\vec{B_j} \tag{2.27}$$

where $\vec{\mu}$ is the magnetic moment, and B is the magnetic field due to neighboring particles.

The magnetic force interactions will also induce a torque on each particle, causing it to rotate as the particles approach (or recede). The magnetic torque, $\vec{\tau}$, is calculated using

$$\vec{M_{i,j}} = \vec{\mu_i} \times \vec{B_j} \tag{2.28}$$

The magnetic interaction energy U is [60]

$$U_{i,j} = \frac{\mu_0}{4\pi}[\frac{\vec{\mu_i} \cdot \vec{\mu_j}}{r^2} - 3\frac{(\vec{\mu_i} \cdot \vec{r})(\vec{\mu_j} \cdot \vec{r})}{r^5}] \tag{2.29}$$

where μ_i and μ_j are the magnetic moments of the i^{th} and j^{th} particles respectively. In the absence of an external field (such as that associated with the local protostar) magnetic dipoles tend to align pole-to-pole, minimizing their interaction energy [41].

2.5 Collisional Cross-section

In order to investigate the influence of various dust parameters on dust coagulation, it is important to examine the collisional cross-section, σ, between two dust grains in proximity to each other. The simplest cross-section is that for ballistic collisions where there are no interparticle forces. In this regime the cross-section is simply

$$\sigma = \pi(a+b)^2 \tag{2.30}$$

where a and b are the radii of the colliding particles.

Analytical calculation of the collisional cross section, σ, between particles which may be charged and/or magnetized is not directly possible as the interactions are not due to a central force. Nevertheless, an expression for σ may be obtained by examining the interaction energy due to the interparticle forces. Following the procedure used for particle motion in a central potentials, such as may be found in Landau and Lifschitz, the scattering of two particles may be described using an effective potential

$$U_{eff} = U_0 + U_L + U_{\vec{p}} + U_{\vec{\mu}} \tag{2.31}$$

where U_0 is the kinetic energy of the particles in a one-body system, and U_L, $U_{\vec{p}}$, and $U_{\vec{\mu}}$ are the interaction energies due to the Lorentz force, electric dipole and magnetic dipole forces respectively, as determined by

$$\begin{aligned} U_L &= \int q[\vec{E} + (\vec{v} \times \vec{B})]dr \\ U_{\vec{p}} &= \int (\vec{p} \cdot \nabla)\vec{E}dr \\ U_{\vec{\mu}} &= \int (\vec{\mu} \cdot \nabla)\vec{B}dr \end{aligned} \tag{2.32}$$

where the integrations run over dr as particles are assumed to approach in essentially a straight line from infinity. Angular deviations at small distances do not introduce appreciable error to the integration as a whole, and so are neglected.

For a generalized system the effective potential will take on the form

$$U_{eff} = \frac{\bar{m}b^2v_\infty^2}{2r^2} + \frac{kq_iq_j}{r} + \frac{k}{r^2}[q_jp_icos(\alpha)sin(\beta) - q_ip_jcos(\alpha')sin(\beta')] - \frac{2kp_ip_j}{3r^3}[sin(\beta)sin(\beta')cos(\alpha+\alpha') - \frac{cos(\alpha)cos(\beta)cos(\beta')}{sin(\alpha)}] - \frac{\mu_0\mu_i\mu_j}{4\pi r^3}[sin(\phi)sin(\phi')cos(\theta+\theta') + cos(\phi)cos(\phi')] \quad (2.34)$$

where $\bar{m}$ is the reduced mass of the interacting particles, b is the impact parameter, v_∞ is the relative velocities of the particles when they are far away from each other, and r is the separation distance. For charged particles, q and $\vec{p}$ denote the charge and electric dipole, and α, β, α', and β' are the polar and azimuthal angles between the electric dipoles and an arbitrary coordinate system. For magnetic particles, μ is the magnetic dipole, and θ, ϕ, θ', and ϕ' are the polar and azimuthal angles between the magnetic dipoles and the same arbitrary coordinate system.

Assuming $U_{eff} = 0$ at infinity, and by using the conservation of energy, assuming particles stick at the point of contact ($R = a + b$), then Equation 2.27 may be set equal to the initial kinetic energy. By requiring the angles between dipoles to be approximately zero (minimization of both electric and magnetic energy) the maximum impact parameter for particle collision is

$$b_{max}^2 = 4R^2[1 - \frac{kq_iq_j}{\bar{m}v_\infty^2R} - \frac{k(q_jp_i - q_ip_j)}{\bar{m}v_\infty^2R^2} + \frac{2kp_ip_j}{3\bar{m}v_\infty^2R^3} + \frac{\mu_0\mu_i\mu_j}{4\pi\bar{m}v_\infty^2R^3}] \quad (2.35)$$

Note that this is an over simplification of the interaction energy as simultaneous alignment of both the electric and magnetic dipoles is not probable. Thus it may be seen that, by using $\sigma_{geo} = 4\pi b_{max}^2$, monopole electric interactions will reduce the

collisional cross section, while dipole interactions enhance it. In the limiting case of high velocities, $v_\infty \to \infty$, then the interaction cross section reduces simple to the geometric cross section.

In the absence of magnetic interactions, assuming particles of equal charge (and dipole moment) the cross-section interaction reduces to

$$\sigma_E = \pi R^2 (1 - \frac{k q_i q_j}{\bar{m} v_\infty^2 R} + \frac{2 k p_i p_j}{3 \bar{m} v_\infty^2 R^3}) \tag{2.36}$$

which is in agreement with the cross section derived by Landau and Lifshitz [61], with the addition of the dipolar term. In the case of magnetic interactions without charging the cross section my be written as

$$\sigma_\mu = \pi R^2 (1 + \frac{\mu_0 \mu_i \mu_j}{4 \pi \bar{m} v_\infty^2 R^3}) \tag{2.37}$$

which agrees with the magnetic cross section as defined by Nubold and Glassmeier [41].

CHAPTER THREE

Numerical Methods

The evolution of dust grains based on varying environmental parameters and grain properties may be studied through a variety of simulations. This work examines aggregation through the use of two different numerical methods: via pair-wise interactions (in which only the target and incoming particles are simulated) and using an N-body simulation (where thousands of particles may be simulated concurrently).

The original code, which modeled gravitational interactions, called box_Tree, was modified by Matthews to include electrostatic interactions [77]. The structure of this code was the adapted to create a new pair-wise interaction code called *Aggregate Builder*, these codes are described in Sections 3.1 and 3.2. The numerical algorithm for charging aggregate structures, OML_LOS is presented in Section 3.3. Quantification of the morphology and gas-grain interactions of aggregates is determined by calculation of physical parameters such as the porosity, compactness factor and friction time. Descriptions of these quantities are presented in Section 3.4.

3.1 Aggregate Builder

Aggregate Builder is a numerical simulation in which aggregates are grown via pair-wise interactions between individual monomers and/or aggregated clusters of monomers. Collisions proceed by placing an initial seed particle, m_1, at the origin of a center of mass frame of reference. An incoming particle of mass m_2, approaches from a randomly selected direction with relative velocity, $\vec{v}$. Incoming particles are initially vectored towards the center of mass of the target particle, plus an offset, called an impact parameter, which may range from zero (no offset) to half of the sum of the radii of the two particles.

Charging and magnetization of particles may be incorporated into the parameters to model different situations of physical interest. When present, charges and electric/magnetic dipoles are included in the parameter space of the interacting particles. The electric field of each particle is approximated using the monopole and dipole terms, while the magnetic field is approximated only to the dipole terms (no magnetic monopoles). Higher order expansions, such as the quadrupole, have been found to have no significant effect on coagulation, and have therefore been neglected.

Force interactions for each particle based on the included parameter space are summed, $\vec{F}_i = \vec{F}_{e,i} + \vec{F}_{\mu,i}$, where $\vec{F}_{e,i}$ includes both monopole and dipole terms, and $i = 1, 2$ includes both particles. Working in the COM frame of the target particle, the acceleration due to the force interactions are combined and then assigned to the incoming particle, $\vec{a} = -\vec{a}_1 + \vec{a}_2$. Assigning the target particle's acceleration to the incoming particle has been found to have no effect on the coagulation of populations, and is used for computational simplicity.

Electric and magnetic dipole moments will also produce a torque, due to their interaction with the associated field from the pair particle, about the particle's center of mass, given by Equations 2.24 and 2.27. The resulting rotation of the aggregates is calculated via Euler's equations

$$\begin{aligned} I_1\dot{\omega}_1 - \omega_2\omega_3(I_2 - I_3) &= N_1 \\ I_2\dot{\omega}_2 - \omega_3\omega_1(I_3 - I_1) &= N_2 \\ I_3\dot{\omega}_3 - \omega_1\omega_2(I_1 - I_2) &= N_3 \end{aligned} \tag{3.1}$$

where $I_i (i = 1, 2, 3)$ are the principal moments of inertia of the aggregate and the $\omega_i\,'s$ are the spin components as measured with respect to the body axes.

As particles rotate and collide, the orientation of the body axes with respect to the stationary space frame, in which the particles are placed, changes with time,

as determined by

$$\begin{aligned}\hat{p}_1 &= \omega_3\hat{p}_2 - \omega_2\hat{p}_3 \\ \hat{p}_2 &= \omega_1\hat{p}_3 - \omega_3\hat{p}_1 \\ \hat{p}_3 &= \omega_2\hat{p}_1 - \omega_1\hat{p}_2\end{aligned} \tag{3.2}$$

where $\hat{p}_i\,'s$ are the unit vectors ascribed to each of the principal body axes.

Calculation of the particle's position, velocity, spin, and orientation is done by means of an adaptive fifth order Runge-Kutta integrator, with a collision check performed at the conclusion of each time step. Collisions are detected when monomers within each aggregate are determined to physically overlap. Once particles have come into contact, the monomers are assumed to stick together at the point of contact, an applicable assumption for low velocity regimes. The particles are then combined into a single new particle with a new center of mass, moments of inertia, spin, charge and electric/magnetic dipoles. The electric charge and dipoles for aggregates are calculated based on the OML_LOS method, described in Section 3.4. Magnetic dipoles are taken as the simple vector sum of the all the constituent magnetic dipoles within each aggregate.

Interactions which do not result in a collision are detected when the particles are receding from each other ($\vec{r} \cdot \vec{v} > 0$, where $\vec{r}$ and $\vec{v}$ are the position and velocity of the incoming particle's center of mass) and are separated by more than $10r_{max}$, where r_{max} is the distance from the seed particle's center of mass to the furthest monomer, enclosing all constituent monomers within this radius.

Aggregates are grown to sizes of $N \approx 2000$ monomers in a series of three generations. First generation ($N \leq 20$) aggregates build solely through the addition of incoming monomers, termed particle-cluster aggregation (PCA). Subsequent to each collision, aggregate characteristics are saved to a particle library for later use. Second generation aggregates are built up to size $N = 200$ through collisions between

aggregates randomly selected from the first generation library, termed cluster-cluster aggregation (CCA). In this aggregation regime, both the seed and incoming aggregates are $2 \leq N \leq 20$. Finally, third generation aggregates are built to the final size, $N = 2000$, by collisions between first and second generation aggregates. Attempted collisions occur until the number of monomers exceeds the maximum number for that generation or the number of missed collisions reaches a preset limit.

3.2 Box Tree

To simulate the evolution of large populations of dust particles a different numerical method is employed, based on the original box_tree code developed by Richardson [62, 63, 64] to model the dynamics of a large number of particles in a protoplanetary disk or ring system through gravitational forces. Additional modifications to the code have been made to allow for charging and magnetization of grains, electrostatic Debye shielding, and external magnetic fields [20]. Box_tree is a combination of two computer algorithms, a box code and a tree code. The box code permits distant regions of a system to be represented by copies of the simulated region. In addition, the box code provides the external potentials acting on grains, specifies a coordinate system, allows for linearized equations of motion in a rotating frame, and provides a prescription for handling boundary conditions [65].

The tree code [66] provides a method for the fast calculation of interparticle forces via multipole expansion. Interparticle forces are treated as a pertubation to the equations of motion. By using this code, a full treatment of rigid body dynamics, including rotations, is possible permitting both cluster trajectories and orientation of aggregates to be tracked.

Treatment of the tree component of the code proceeds by division of the box into 2^n cells, where n is the number of dimensions of the box. Each cell is further divided into 2^n cells, until each cell contains a single particle. Cells sufficiently far

away from the grain of interest, defined by a critical opening angle, use a multipole expansion to calculate the self-gravitational, electrostatic and magnetostatic forces on the grain [63]. Forces due to cells proximal to the grain in question are directly calculated without use of a multipole expansion. Multipole terms for the self-gravitational, electrostatic and magnetostatic forces of the tree structure are expanded about a cell's center of mass.

Debye shielding of grain potentials is incorporated into the code by a screening factor used to scale the electrostatic force

$$\vec{F'}_e = \vec{F}_e(1 + \frac{r}{\lambda_D})e^{-\frac{r}{\lambda_D}} \tag{3.3}$$

where λ_D is the Debye length of the plasma, and r is the distance from the grain.

Outcomes of collisions depend strongly on the energies involved. When two particles collide, they may stick, bounce, crush, melt, slide or fragment. The physics of collision processes have been developed and examined by various studies, such as those performed by Chokshi et al. as well as Dominik and Tielens [67, 16]. For sticking to occur when grains come into contact their velocity must be lower than some critical value, v_{cr}.

At low velocities particles to form aggregates, where colliding particles stick together at the point of contact. Linear and angular momentum are conserved during the collision via use of Euler's equations as applied to rigid body rotation.

Spherical particles which become charged will have ions and electrons evenly distributed over the surface with a potential equivalent to that of a point charge at the COM of the particle. More complex structures have charges arranged over the surface in order to minimize the overall surface potential. Due to the computational complexity of explicitly calculating the exact potential of each aggregate within an N-body simulation an approximation of the charge distribution is expedient.

3.3 Numerical Charging of Aggregates

Dust grains in astrophysical environments are constantly undergoing formation processes such as coagulation, condensation and nucleation, as well as destruction processes, such as sputtering, fragmentation and vaporization [68]. Due to the irregular and fractal structures, calculation of the charge on aggregates requires numerical simulation. The current numerical method utilized in this study is *OML_LOS* (Orbital Motion Limited- Line of Sight), which simulates the charging of monomers and aggregate structures. This code was originally developed by Hayes *et al.* to simulate the charging of aggregates immersed in plasma environments by determining open Lines of Sight (LOS) to patches on the aggregate surface [69]. Subsequently, secondary electron emission and UV radiation were added to the code by Ma *et al.* to simulate a wider range of astrophysical charging environments [70]. Most recently, the code has been modified to incorporate the charging of non-spherical monomers individually and within aggregate structures, as discussed in Section 3.3.4.

3.3.1 Charging Current Density

The electron and ion currents given by the basic charging equations for spheres are not applicable to arbitrary or irregularly shaped objects. For such cases, the surface area of the object requires a numerical approximation, achieved by using a set of discrete points or surface elements on the structure. To determine the charge, a calculation of the current density to each element is needed. This method may be used to calculate the plasma current, secondary electron and/or the photoelectric current densities.

Current densities due to each species within a plasma (electrons and ions) are calculated by

$$J_{e,i} = \int q_{e,i} \vec{v_{e,i}} f^*_{e,i}(\vec{v_{e,i}}) d^3 \vec{v_{e,i}} \tag{3.4}$$

where $f*(\vec{v_{e,i}})$ is the modified Maxwellian distribution which includes the potential

energy of the electrons and ions, given by

$$f^*_{e,i}(\vec{v_{e,i}}) = n_{e,i}(\frac{m_{e,i}}{2\pi kT_{e,i}})^{3/2} exp(-\frac{m_{e,i}v^2_{e,i} + 2q_{e,i}\phi_s}{2kT_{e,i}}) v^2_{e,i} dv_{e,i} d\Omega \tag{3.5}$$

By employing Equation 3.5 in Equation 3.4, separating the angular integrations, and integrating over the velocity, the current densities are seen to be

$$\begin{cases} J_{e,i} = n_{e,i}q_{e,i}\sqrt{\frac{kT_{e,i}}{2\pi m_{e,i}}}\frac{1}{\pi} exp(-\frac{q_{e,i}\phi_s}{kT_{e,i}}) \int\int cos\theta d\Omega, \;\; q_{e,i}\phi_s \geq 0 \\ J_{e,i} = n_{e,i}q_{e,i}\sqrt{\frac{kT_{e,i}}{2\pi m_{e,i}}}\frac{1}{\pi}(1 - \frac{q_{e,i}\phi_s}{kT_{e,i}}) \int\int cos\theta d\Omega, \quad q_{e,i}\phi_s < 0 \end{cases} \tag{3.6}$$

The only difficulty remaining is determining the limits of integration for the angular integrals. The numerical method for determining $\int\int cos\theta d\Omega$, called the line-of-sight factor, will be discussed in Section 3.2.2.

3.3.2 LOS Algorithm

Calculation of the charge on dust grains is done by determination of the current densities, as described in Section 2.2, and the portion of the solid angles which is open for ions and electrons to scatter off of dust grains. Calculating the current density on dust grains requires integration over $\int\int cos(\theta)d\Omega$. For a sphere, this integration is straight forward, $\int_{-\pi/2}^{\pi/2}\int_0^{2\pi} cos(\theta)d\Omega = \pi$. In order for this intergration to proceed numerically, the monomer surfaces are divided into a large number of surface patches by division of the polar and azimuthal angles into a finite set of ranges, depicted in Figure 3.1. From the center of each patch a normal vector is determined. For monomers which constitute part of an aggregate this normal vector for each patch is examined to determine whether it passes through any other particle. If so the line of sight from this patch is determined to be blocked, otherwise the line of sight is open and the line of sight may contribute to the overall contribution from the current density. A representation of open and blocked lines of sight is shown in Figure 3.2, where the shaded areas are angles where incoming ions and electrons may collide with the grain surface.

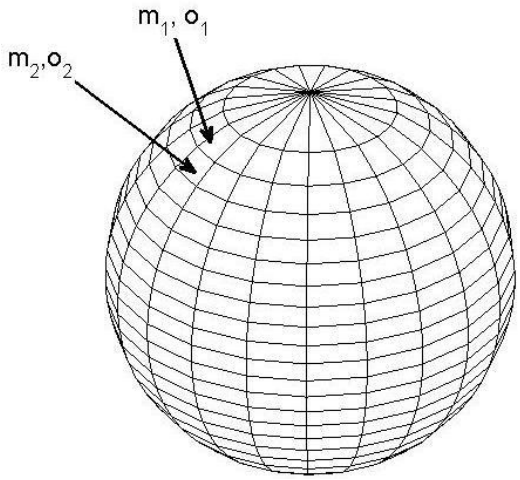

Figure 3.1. Approximation of the surface of a spherical monomer using 420 area patches.

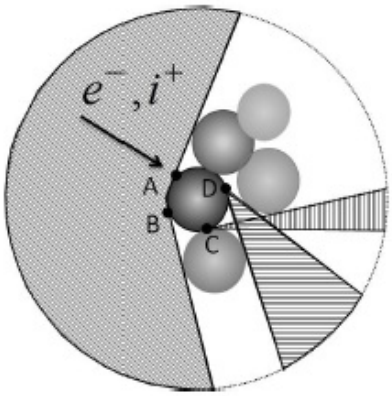

Figure 3.2: Charging currents to a monomer within an aggregates. The open lines of sight to points A, B, C, and D on a monomer are indicated by the shaded regions.

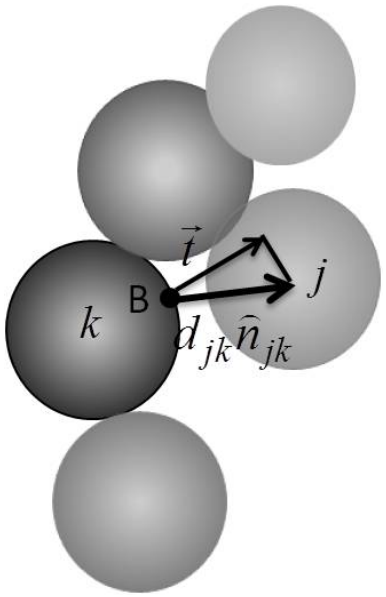

Figure 3.3: Geometry to determine if sample test direction from point B on the surface of a monomer k is blocked by another monomer j.

At the center of each surface patch, test directions, $\hat{t}$, are used to determine open lines of sight. The test direction is said to be blocked if it intersects any other monomer in the aggregates, or the monomer itself ($\mathrm{LOS}_t = 0$), and open otherwise ($\mathrm{LOS}_t = 1$). The geometry of open and blocked lines of sight is shown in Figure 3.3. Mathematically the conditions to determine a blocked line of sight are

$$\begin{aligned} |d_{jk}|^2 - |d_{jk}\hat{n}_{jk} \cdot \vec{t}|^2 < r_j^2 \\ \vec{t} \cdot \hat{n}_{jk} > 0 \end{aligned} \tag{3.7}$$

where r_j is the radius of the j^{th} monomer, and d_{jk} is the distance between the surface patch on monomer k and the center of the monomer j. The projection of $d_{jk}\hat{n}_{jk}$ onto the test direction $\hat{t}$ is used to construct a triangle. If the third side of the triangle is smaller than the radius of particle j, the line of sight is blocked. Note that when $j = k$, $d_{jk} = r_j$, the issue reduces simply to determining $cos\theta_t = \hat{t} \cdot \hat{n}_{jk} < 0$, which is a condition on the velocity subspace.

3.3.3 OML Algorithm

Within the OML_LOS code, the electrostatic potential at each point on the surface is calculated by using the first two terms of a multipole expansion, the monopole and dipole terms, given by

$$\phi(r) = \sum_i \frac{Q_i}{4\pi\epsilon_0 r_i} + \sum_i \frac{\vec{P}_i \cdot \vec{d}_i}{4\pi\epsilon_0 d_i^3} \tag{3.8}$$

where i sums over all the monomers in the aggregate, Q_i and $\vec{P}_i$ are the monopole and dipole moments of the i^{th} monomer, and $\vec{d}_i$ is the position vector from the center of the i^{th} monomer to the center of the surface patch. The total current density is simply the sum of the electron and ion densities, $J_{total} = J_{electron} + J_{ion}$.

In addition to the total incident current densities, it is necessary to calculate the surface area of each patch shown in Figure 3.1. For a sphere the area is given by $dS = r^2\Delta\Omega$. Determination of the area of a surface patch on an ellipsoidal monomer is more complex, but eventually yields a similar factor. With the areas determined the net current density may then be determined by

$$dI = J_{total} \times dS \tag{3.9}$$

Calculation of the total current and dipole moments proceed by summing the current contributions over all of the surfaces patches, give by

$$I_i(t) = \sum dI \tag{3.10}$$

$$\vec{D}_i(t) = \sum I\vec{r}_i \tag{3.11}$$

where $\vec{r}_i$ is the distance from the center of the surface patch to the monomer's center.

The contribution of the total current to the charge and electric dipole moments of aggregates for each monomer is given by

$$dQ_i(t) = I_i(t)dt \tag{3.12}$$

$$d\vec{P}_i(t) = \vec{D}_i(t)dt \tag{3.13}$$

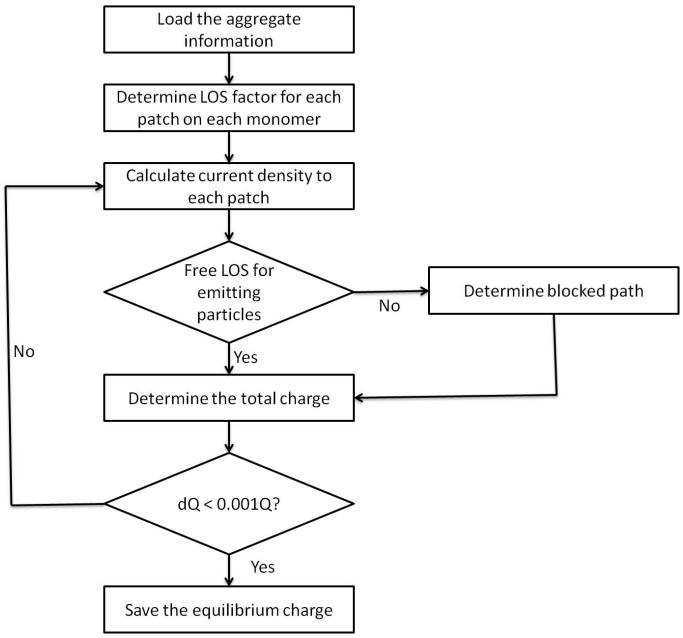

Figure 3.4: Basic scheme of OML_LOS. This image has been reproduced by permission of Ma [71].

where i denotes the i^{th} monomer and dt is the time step. By allowing the time step to advance the total charge and electric dipole moment for the aggregate as a whole may be calculated via

$$Q(t) = Q(t-1) + \sum_i dQ_i(t) \tag{3.14}$$

$$\vec{P}(t) = \vec{P}(t-1) + \sum_i d\vec{P}_i(t) \tag{3.15}$$

The process is iterated in time until $dQ(t) < 10^{-3}Q(t-1)$, essentially when the additional temporal contribution to the charge becomes insignificant, at this point electrostatic equilibrium is assumed to have been achieved. The process of charging aggregates may be summed up schematically with the flow chart shown in Figure 3.4 [71].

3.3.4 Charging of Ellipsoidal Monomers

There charging method described hereto has been optimized for the charging of spherical monomers as the constituents of aggregates. There is evidence however,

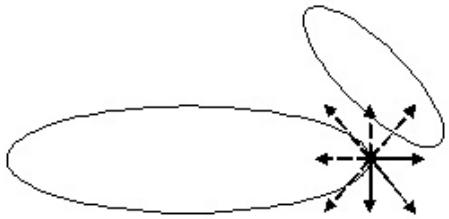

Figure 3.5: Open and blocked lines of sight (LOS) for a patch on an ellipsoidal monomers. Dashed lines represent blocked lines of sight while solid lines indicate open lines of sight, along which electrons and ions may impact the particle.

as presented in Section 5.1, which indicates that not all dust particles are spherical in nature. It is therefore desirable to generalize the numerical method utilized for arbitrary ellipsoidal shapes (with each axis being able to be set independently of the others).

The first mathematical obstacle to overcome is the calculation of the angles between the incoming LOS factors and the normal vector of each surface patch. Because the code works in the COM frame of reference for particles this was a straightforward process for spherical monomers as the normal vector is equivalent to the vector connecting the COM to the center of the surface patch. For ellipsoidal monomers this is not the case (except in the case of the patch being centered about a semi-major or semi-minor axis). The normal vector for each patch can be found by taking the gradient of the equation for an ellipsoid

$$\frac{x^2}{a^2} + \frac{y^2}{b^2} + \frac{z^2}{c^2} = 1 \tag{3.16}$$

where a, b, and c are the lengths of the semi-axis and x, y, and z are the spatial coordinates of the patch being examined. The normal vector is then the normalized gradient using the proper coordinates, from which the angles may then determined in the same manner as for spherical monomers.

A second modification to the charging process for ellipsoids is the calculation of the surface area of the patches. As can be seen in Figure 3.2 equal divisions have

been used for $sin(\theta)$ so that the area of all patches are equal. This simplification allows one value of the surface area to be stored and multiplied by the current density to find the current indicent on a patch. For ellipsoids there is no easy method to divide the polar and azimuthal angles to replicate this simplification. Instead the surface area of each patch must be calculated, and stored, according to

$$SA = \int_{\phi_{min}}^{\phi_{max}} \int_{\theta_{min}}^{\theta_{max}} \sqrt{a^2b^2cos^2(\phi) + c^2(b^2cos^2(\theta) + a^2sin^2(\theta))sin^2(\phi)} d\theta d\phi \quad (3.17)$$

where θ is the azimuthal angle and ϕ is the polar angle.

In order to test the code, all semi-axes were set equal in order to simulate a sphere. The resulting magnitude of the charge was then compared to the charge resulting from using the unmodified OML_LOS code. For spherical monomers ranging in radius from a few nanometers to the micrometer size range the magnitude of the charge was found to agree within 0.01%.

The charge distribution on a prolate ellipsoid with an axes ratio of 3:1:1, as shown in Figure 3.6. Red indicates a positive charge, while blue indicates a negative charge. The color bar is given in units of Coulombs. The total charge on the monomer is $Q = 1.75 \times 10^{-16}C$. One of the chief differences for charged spheres versus ellipsoids is the arrangement of charge on the surface. While the charge is evenly distributed over the surface of a sphere, this does not hold true for ellipsoids due to their varying curvature. Surface charge is preferentially located towards the ends, along the semi-major axis. Along the minor axes there is less negative charge, and even some positive charging in areas. An important consequence of this is that charged ellipsoids have a dipole moment, which is known to increase collision probability. When treating the coagulation of spherical monomers, dipoles interactions only come into play after aggregates are formed.

The code was also tested by charging ellipsoidal monomers with aspect ratios varying from 0.01 to 100. The results were compared to those reported by Auer,

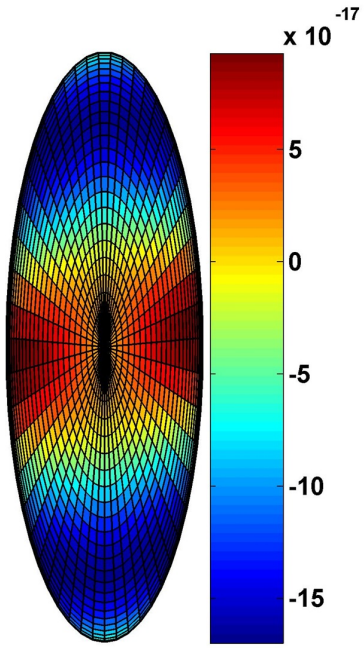

Figure 3.6: Arrangement of charges on a prolate ellipsoidal monomer. The bulk of the negative charges collect on the high curvature ends of the ellipsoid due to their larger LOS factors. This charge arrangement will also lead to a small dipole due to the separation of charges on the ends.

Kempf, and Grun using a commercial software which uses an infinite volume method to solve Maxwell's equations in integral form [72]. Charge on ellipsoids with varying aspect ratios is shown in Figure 3.7. Where the charge on ellipsoidal monomers is normalized by the charge of a sphere of equivalent volume and plotted versus the length/diameter ratio. The results are in good agreement for all tested aspect ratios.

3.4 Approximation of Charge and Electric Dipole Moments on Aggregates

Direction numerical integration of the charge on particles of arbitrary shapes is, as stated previously, computationally tedious. While direct calculation is typically used when employing *Aggregate Builder*, it is not desirable to do so when modeling a large number of particles, as with *box_tree*. In order to effectively model coagulation in the cases of charged monomers and aggregates, it is therefore useful to employ a power law approximation of the charge and electric dipole moment for aggregates for simplicity.

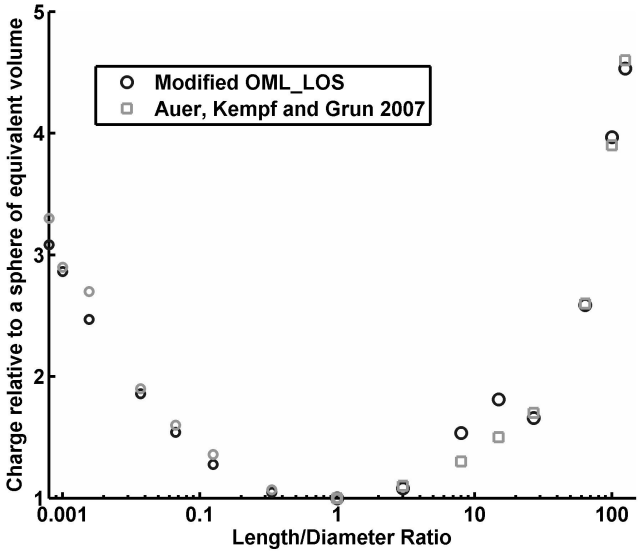

Figure 3.7: Charge ratio versus length/diameter ratio using monomers of constant volume. The charge is seen to increase as the length of the semi-major axis increases

Previous work has shown that the charge and dipole moment for a particle created through a collision may be approximated by [73]

$$Q = \alpha N^{\beta} Q_0 \tag{3.18}$$

$$p = \gamma I^{\delta} p_o \tag{3.19}$$

where Q_0 and p_0 are the sum of the original charges on the monomers and the combined magnitude of the dipole moment, I is the maximum moment of inertia, N is the number of monomers within the new aggregate and α, β, γ, and δ are constants determined by a log-log fit to the charge and dipole moments calculated for aggregate populations. These log-log fits are generated for aggregate populations built using the *Aggregate Builder* code and charged using OML_LOS.

3.5 Physical Analysis

Aggregates grown by models employing varying environments and dust parameters can be analyzed to determine how these parameters affect the rate of aggregate growth, and their interaction with their surrounding environment. For parameters

which may result in an appreciable number of missed collisions, the first concern may be addressed through a simple statistical analysis of the probability of sticking collisions.

The resulting structures and the gas-grain interactions are analyzed by several, parameters: porosity, fractal dimension, compactness factor, and friction times. Each of these quantities addresses a different aspect of aggregate behavior and are described below.

3.5.1 Porosity

The porosity of aggregates is a direct measure of how much open space is contained within an aggregate of radius R_{max}, where R_{max} is determined by the furthest extent of the aggregate from its COM. The porosity of an aggregate structure is defined as

$$p = 1 - \frac{V}{V_T} \tag{3.20}$$

where V is the total volume of the constituent monomers ($V = \sum V_i$, with V_i being the volume of individual monomers), and V_T is a volume of a sphere with a radius equal to the radius of gyration, as determined by the principal moment of inertia. For monodisperse populations of dust grains, this equation may be reduced to

$$p = 1 - N(\frac{r}{R_c})^3 \tag{3.21}$$

where r is the radius of a spherical monomer, or the geometric mean radius of an ellipsoidal monomer, N is the number of monomers within the aggregate, and R_c is the characteristic radius of the aggregate, which is related to the radius of gyration by $R_c = \sqrt{\frac{5}{3}} R_g$.

Porosities run between $0 < p \leq 1$, where high porosities imply large amounts of empty space within an aggregate. Lower porosities correspond to space within the aggregate being filled, leading to denser structures as the porosity decreases.

3.5.2 Fractal Dimension

The fractal dimension provides a measure of the openness of an arbitrarily shaped structure. The fractal dimension may range from unity for an open, linear structure, to three for a compact sphere. The fractal dimension is thus an important parameter for collisional processes since fluffy, extended aggregates will obviously exhibit a much higher collisional cross-section. At the same time, open porous structures are in general entrained in the gas in which they are immersed, which may suppress the relative velocities between grains, reducing coagulation rates.

To calculate the fractal dimension an aggregate is enclosed within a cube with sides of length a divided into a_0^3 sub-boxes. The number of sub-boxes containing a portion of the aggregate is given by $N(a_0)$ allowing the fractal dimension to be calculated by

$$F_d = \frac{log(N(a_0))}{log(a_0)} \tag{3.22}$$

3.5.3 Compactness Factor

Aggregate growth leads to highly varied structures in comparison to the shape of the constituent monomers. Another parameter used to describe the aggregate structure is the compactness factor, denoted by Φ, which is a ratio of the volume of the constituent monomers to the volume of a sphere with a radius defined by a projected geometric cross-section [74]

$$\Phi_\sigma = \frac{\Sigma r_i^3}{R_\sigma^2} \tag{3.23}$$

where r_i is the radius of individual monomers, and the sum runs over all monomers within an aggregate, and R_σ is the radius of the average projected cross-section, defined as

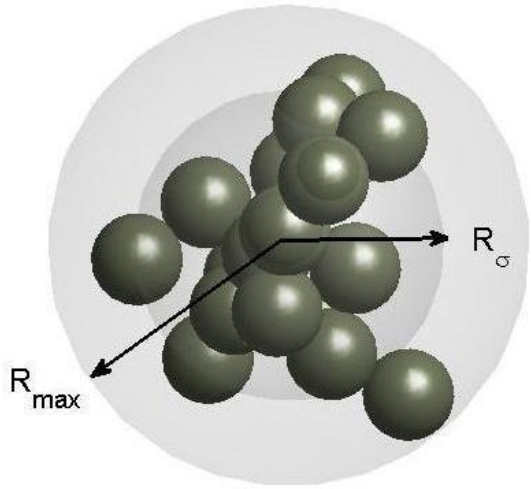

Figure 3.8: An illustration of the compactness factor. The exterior shaded circle corresponds to the maximum radius of the aggregates, R_{max}, while the darker, inner shaded region corresponds to R_σ. For more compact structures, the ratio of the volumes approaches unity. For more open structures, the ratio of the volumes approaches zero.

$$R_\sigma = \sqrt{\frac{\sigma}{\pi}} \tag{3.24}$$

with σ being the projected cross-section averaged over several orientations to reduce variance. For non-spherical particles, $r_i^3 = abc$, where a, b, and c are the semi-axes of the monomer. Figure 3.8 shows a representative aggregate, built from monodisperse spherical monomers, with R_σ and the maximum aggregate radius R_{max} indicated. For very compact (spherical) structures, Φ_σ approaches a limiting value of unity. Lower compactness factors, tending towards zero, indicate very open, fluffy structures.

3.5.4 Friction Time

In the absence of turbulence and interparticle forces the motion of dust grains in a plasma enviroment in dominated by the behavior of the gas in which they are immersed. The measure of this coupling between dust grains and gas is given by the friction time, which is defined by Armitage as [48]

$$\tau_f = \frac{m}{\sigma}\frac{1}{\rho_g v_{th}} \tag{3.25}$$

where m is the mass of the particle, σ is the cross-sectional area of the aggregate, ρ_g is the density of the gas and v_{th} is the thermal sound speed.

The strength of the coupling between dust grains largely determines the movement of aggregates. Short friction times mean aggregates are well coupled to the gas motions, and quickly return to the average eddy velocity after any stimuli (such as collisions). Longer friction times allow for particles to take longer to return to their median speed, permitting larger relative velocities with nearby particles, which increases the probability of further coagulation.

If turbulence is assumed to be present in the region of concern, as discussed in Section 2.1.3, then dust particles may have a broad range of relative velocities. The relative velocities between aggregates induced by turbulent motion for small grain sizes is proportional to the difference between friction times, $\Delta V \propto \tau_1 - \tau_2$. Thus the greater the difference in the magnitude of friction times within a population of aggregates, the greater relative velocities which may be achieved through turbulent motion, and more likely collisions are to occur.

CHAPTER FOUR

Electromagnetic Dipole Interactions

Portions of this Chapter have been published as "Dipole-Dipole Interactions of Charged-Magnetic Grains" *IEEE Trans. on Plasma Sci.* 38(4):792-797, 2010.

4.1 Pair-wise Interactions

To begin, the effect of charged-magnetic grains on the coagulation of dust particles will be examined. The results obtained from numerically growing aggregates will be compared to previous studies of both charged aggregates and aggregates formed from magnetic materials [41, 77]. The primary purpose of this effort is to further the exploration of aggregation under the influence of both charge and magnetization in order to gain a better theoretical understanding into the basic physics of teh aggregation process while looking into the effect a grain's charge and mangetic dipole moment affect this process. The effects will be characterized through the calculation of collision probability, fractal dimension and the morphology of the resultant aggregates.

4.1.1 Initial Conditions

Using *Aggregate Builder* four different monomer parameter sets were examined: 1) Magnetic grains, 2) Charged grains, 3) Charged-magnetic grains, and 4) Uncharged grains with no magnetic moment. In each simulation the size and density of the constituent monomers were assumed to be that of iron grains with radii of $r = 20$ nm and mass $m = 2.66 \times 10^{-19}$ kg. Magnetic grains (with or without charge) were given a magnetization of $\mu = 7 \times 10^{-18} A \cdot m^2$.

Velocities of incoming particles were set according to Equation 2.1, with $T =$ 100 K. Incoming velocities for magnetic grains randomly ranged from the thermal

velocity, v_{th}, down to $v_{th}/16$ in order to match initial conditions from Dominik and Nubold [42]. For charged and charged-magnetic populations, speeds ranged from $2v_{th} \leq v \leq 5v_{th}$. These higher speeds were required to overcome the Coulomb repulsion between particles. The plasma temperature was set such that a monomer charged to a potential of $V = -0.0707$ V.

4.2 Results

4.2.1 Charge and Dipole Moments

During collisions the magnetic dipoles of grains tend to align as the particles approach each other, upon collision the dipole moment is assumed to be "frozen in" contributing to the total magnetic dipole moment of the entire aggregate. Figure 4.1 shows the normalized magnetic moment of a cluster, μ/μ_0, where μ_0 is the magnetization of a single grain, as a function of aggregate size, N, for a population where only magnetic interactions are present. The trend line indicates the magnetic moment increases as $\mu \propto N^{0.53}$, similar to previously published results [41]. This is in contrast to the electric dipole moment, which is only weakly dependent on N. The magnetic dipole moment tends to grow with the addition of each monomer or aggregate, as the magnetic dipoles tend to align independent of the point of collision. The electric dipole, on the other hand, is determined by the plasma flux to unblocked surfaces of monomers within an aggregate, and thus depends most strongly on the final geometry of the aggregate, instead of size.

Growth of the magnetic dipole has also been examined for aggregates grown from charged-magnetic grains, Figure 4.2. Again, the magnetization has been normalized by the magnetic dipole moment of a single monomer, μ_0. Trend lines indicates that the magnetic dipole moment increases as $\mu \propto N^{0.68}$, indicating a rate of growth in excess of that seen for a purely magnetic population. This additional alignment of dipoles is due to the small collisional velocity between particles.

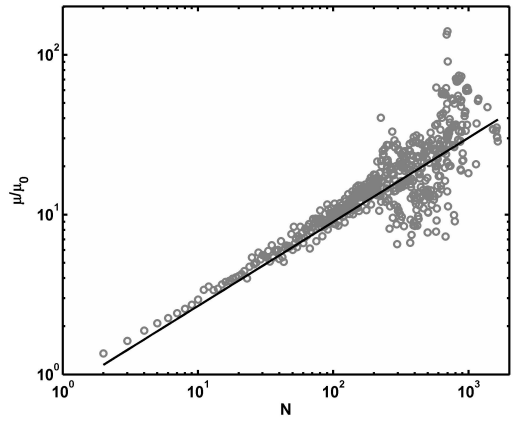

Figure 4.1: Normalized cluster magnetic moment as a function of N, the number of monomers in an aggregate. The fit line shows an exponential increase $\mu \propto \mathrm{N}^{0.53}$.

The aggregate charging model yielded fits for charge and electric dipole moments (Equations 3.18-3.19) of

$$Q = 0.98N^{0.50}q_0 \tag{4.1}$$

$$|p| = 0.10N^{-0.12}|p_0| \tag{4.2}$$

for the charged population and

$$Q = 0.99N^{0.46}q_0 \tag{4.3}$$

$$|p| = 0.09N^{-0.10}|p_0| \tag{4.4}$$

for the charged-magnetic population. It may be seen from Equations 4.1-4.4 that the charge and electric dipole moments evolve very similarly for both populations, although charged-magnetic aggregates will have slightly reduced charge and dipoles. This difference between the two sets of parameters is due to the structural variation induced by the inclusion of the magnetic dipole interaction.

4.2.2 Collision Probability

Collision statistics for each potential interaction were collected including collision outcome, initial velocity, impact parameter, and the size of the particles (N).

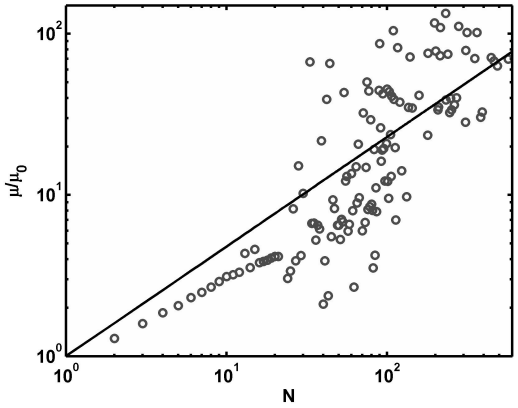

Figure 4.2: Normalized magnetic moment of clusters as a function of N. The fit line shows an increase in dipole moment of $\mu \propto N^{0.68}$, greater that seen in Figure 4.1 for purely magnetic interactions.

These statistics were then used to determine the probability of interaction and coagulation between particles under the initial conditions described previously.

Collision probability statistics were examined as a function of relative velocities between particles as shown in Figure 4.3. Incoming magnetic aggregates (Figure 4.3a) show a high probability of colliding with the target aggregate for all velocities up to the maximum permitted velocity. At lower speeds, magnetic grains allow alignment of the magnetic dipoles which in turn enhances collision probability by supplying an attractive force between the particles. As expected, missed collisions occurred most often at higher velocities, where sufficient dipolar alignment is prevented by smaller interaction times. These high speeds for magnetic particle result in behavior reminiscent of ballistic coagulation.

As mentioned above, both charged and charged-magnetic grains were given higher initial velocities in order to overcome Coulomb repulsion. For the size regimes of grains modeled, the minimum collisional velocity between monomers is approximately $3v_{th}$. Below this threshold, both populations exhibited a very low collision probability. From Figure 4.3b it can be seen that charged-magnetic grains exhibit a higher probability of coagulation at speeds greater than $3v_{th}$, evidently due to

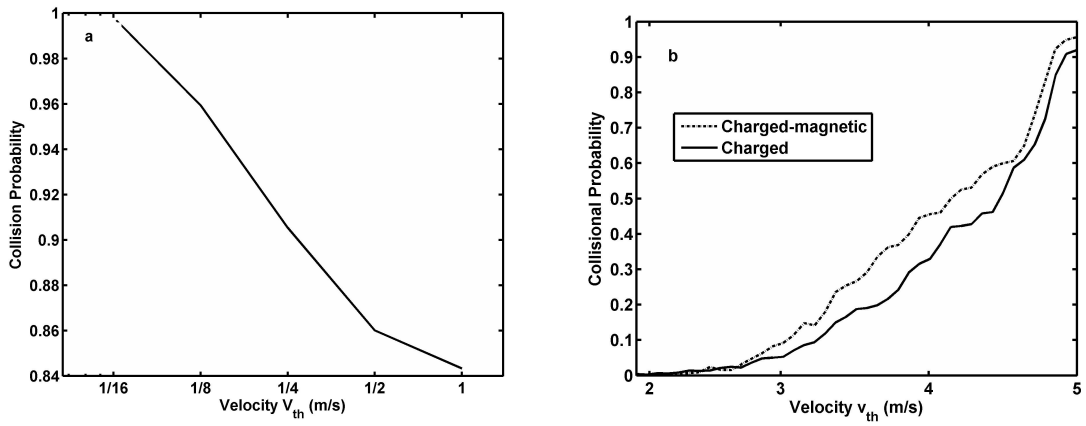

Figure 4.3: a) Probability for collision of magnetic grains having an initial speed of $1/16v_{th} \leq v \leq v_{th}$, b) Probability of collision for charged and charged-magnetic aggregates having an initial speed of $2v_{th} \leq v \leq 5v_{th}$.

coagulation being enhanced by the of the addition attractive force due to the magnetization. The maximum difference between collision probabilities for the two populations is $\sim 12\%$ at speeds between $3v_{th}$ and $4v_{th}$. At the highest speeds examined (above $4.5v_{th}$) the collision probabilities become similar once again, approaching a limiting value of unity. At those speeds the collisions between grains are similar to ballistic collisions, matching the collision probabilities of magnetic grains at high speeds.

When examining collision probabilities as a function of impact parameter, the difference between charged and charged-magnetic grains is less pronounced than when examining the relative velocity, Figure 4.4. Impact parameters with values less than R_{max} yield an appreciably higher collision probability for charged-magnetic grains as compared to charged grains. However, for larger impact parameters both grain types exhibit similar collision probabilities, which is only slightly enhanced by the addition of magnetization. This is in large part due to the short-range nature of the dipole-dipole interactions. Collision probabilities for neutral grains undergoing ballistic coagulation are shown in Figure 4.4 as well, with the collision probability essentially unity for impact parameters up to the grazing distance between two

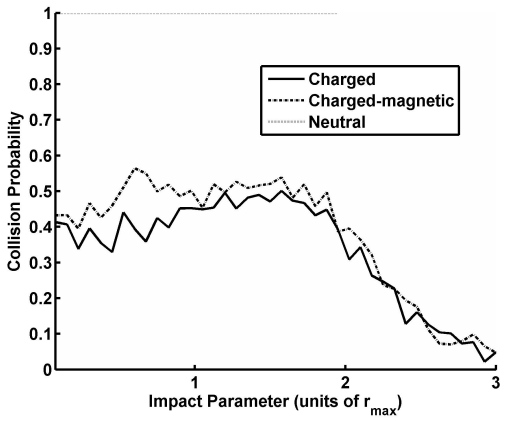

Figure 4.4: Collision probability for charged, charged-magnetic, and neutral grains vs. impact parameter.

particles, $b = 2R$, and zero beyond that. This is due to the compact nature of neutral aggregates.

4.2.3 Fractal Dimension

Aggregates built from the four parameter sets were analyzed for their fractal dimensions according to the method in Section 3.5.2. Aggregates assembled from magnetic material tend to form filamentary structures consisting of many linear chains. Such structures have been created and observed in previous laboratory experiments [75]. Magnetic grains tend to form these chains through the alignment of the magnetic dipoles of local chains. Similar linear structures can be seen within the typical small aggregate formed from these numerical simulations as shown in Figure 4.5a. Larger aggregates composed of magnetic grains are less linear; however the total structure still consists of linear chains most easily seen at the periphery of the aggregate (Figure 4.5b). A greater induced spin on an incoming monomer or aggregate reduces the dipole alignment in the resultant aggregate. For magnetic populations this also reduces the linear nature of any resulting aggregate structures.

Charged monomers tend to form a denser, more compact structure as can be seen in Figures 4.5c-d. Charged-magnetic grains exhibit a behavior intermediate to

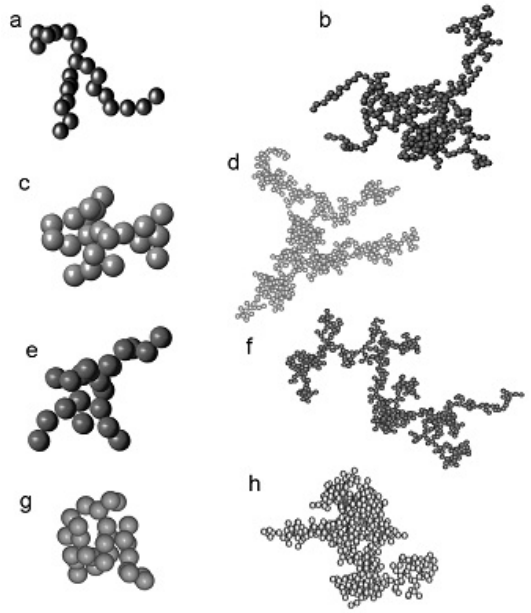

Figure 4.5: Comparison of aggregates formed from the following populations: a-b) Magnetic aggregates of $N = 22, F_d = 2.159$ and $N = 334, F_d = 1.789$ respectively. c-d) Charged aggregates with $N = 21, F_d = 2.333$, and $N = 595, F_d = 1.907$ respectively. e-f) Charged-magnetic aggregates of $N = 21, F_d = 2.359$, and $N = 504, F_d = 1.819$. g-h) Neutral aggregates with $N = 25, F_d = 2.403$ and, finally, $N = 589, F_d = 1.976$.

both magnetic and charged aggregates, as expected (Figures 4.5e-f). While branches are more clumped than those for magnetic aggregates, they are decidedly more linear than an equivalent non-magnetic charged structure (Figure 4.5d). Neutral grains form relatively dense and more spherical aggregate structures at all sizes, as seen in Figures 4.5g-h.

The fractal dimension for each population of aggregates as a function of N is shown in Figure 4.6. The best-fit lines are shown only including data for aggregates with $N \geq 10$. A general decrease in fractal dimension can be seen as N increases, as large aggregates have a more porous structure than do small aggregates, which consist of only a few spherical monomers. Uncharged aggregates formed from magnetic material exhibit the lowest fractal dimension, as expected. It is interesting to note that while the charged grains and charged-magnetic grains have nearly identical fractal dimensions for the smaller aggregates ($10 \leq N \leq 20$), the charged-magnetic

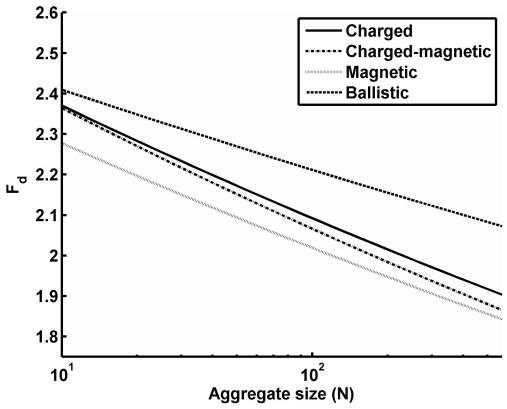

Figure 4.6: A comparison of the average fractal dimension for each population of aggregates as a function of size. Each line is a best fit to the fractal dimension of all aggregates with $N \geq 10$ in a given population. Error bars have been omitted for clarity.

aggregates tend towards lower fractal dimensions for larger N, exhibiting an increasingly open structure. This open structure is due to the existence of local linear chains of monomers in the magnetic aggregate structures. These linear chains are formed through the alignment of the magnetic dipole moments during coagulation for a single incoming monomer. This indicates that the magnetic force between aggregates becomes increasingly important relative to the electrostatic interactions, largely due to the the steady increase of the magnetic moment with increasing N (c.f. Figure 4.1) while the electrostatic dipole moment is only weakly dependent on N. Aggregates constructed from ballistic collisions tended to have the largest fractal dimensions at all sizes.

Probability density estimates for fractal dimension were also calculated for each population as shown in Figure 4.7. Analysis was done using an equal number of second- and third-generation grains from each population; first generation aggregates were not included because of the similarity of fractal dimensions at low N across all four populations. As shown in Figure 4.7a, magnetic aggregates have a local maximum at a lower fractal dimension when compared to other populations, centered at approximately $F_d = 2.05$, with a significant percentage, 36.5%, of the

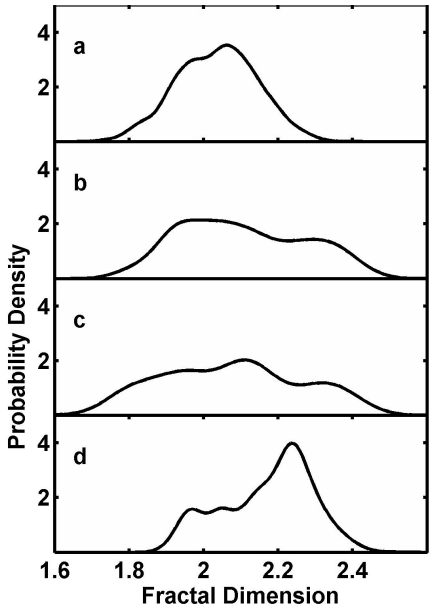

Figure 4.7: Probability density estimates for the fractal dimensions of each population. a) Magnetic grains exhibit a local maximum at $F_d = 2.05$. b) charged aggregates have a broad distribution in fractal dimension. c) Charged-magnetic aggregates also show a broad distribution similar to charged aggregates, but have a larger percentage of aggregates with $F_d < 2.0$. d) Neutral aggregates have a relatively narrow peak at $F_d = 2.25$.

aggregates with fractal dimensions less than 2.0. Charged and charged-magnetic grains, Figured 4.7b-c, show a much broader range of fractal dimensions. Charged-magnetic grains do, however, have a greater percentage of aggregates with fractal dimensions at the lowest fractal dimensions ($F_d < 2.0$), 36.5% for charged-magnetic and 32.4% for charged aggregates, and a smaller percentage of aggregates with large fractal dimensions ($F_d > 2.2$), 27.1% for charged-magnetic and 30.8% for charged grains, respectively. This indicates the influence of the magnetic interactions on the coagulation process. Neutral grains (Figure 4.6d) show a narrow peak near $F_d = 2.25$, a larger fractal dimension than for any of the other populations. The neutral population has essentially zero aggregates form with the lowest fractal dimensions ($F_d \leq 1.8$).

4.3 Magnetic Contribution to Pair-wise Aggregation

In the previous section a comparison between aggregate structures resulting from collisions between magnetic and non-magnetic, charged and uncharged dust grains was been presented. Initial simulations suggest that aggregate populations assembled from charged-magnetic grains exhibit behavior intermediate to that shown by aggregates assembled from purely charged or magnetic grains, as expected. This behavior can be clearly seen in both the collision probabilities between aggregates as shown in Figured 4.3 and 4.4, and the fractal dimension of the resulting aggregates as seen in Figures 4.5-4.7.

The collision probability for populations grown from charged and charged-magnetic grains leads to the conclusion that the charge on the grains is the most significant factor determining the behavior of the aggregates, especially for small N. On the other hand, magnetization of the grains provides an attractive force between aggregates which can lead to a higher probability of a sticking collision. This difference is most pronounced for low velocities (but still with velocities large enough to overcome Coulomb repulsion) and small impact parameters. Magnetic forces play an increasingly important role in determination of the fractal dimension for large aggregates, which follows from the increase of the magnetic moment seen in Figurse 4.1 and 4.2.

The results of studying pair-wise interactions imply that the physical structure of aggregates may be tuned by appropriate selection of initial monomer properties in addition to environmental parameters. This is of great benefit when attempting to replicate known conditions within astrophysical environments as well as the study of coagulation within an laboratory setting. However, the study of these interactions must be expanded to a large number of particles interacting simultaneously to examine whether such behavior scales with the number of particles. This will be examined in the remainder of this chapter.

4.4 N-body Dipole-Dipole Interactions

4.4.1 Initial Conditions

Similar to the pair-wise study, four dust populations are examined; each population consisting of a mixture of iron and silicate material based on meteoric evidence of the composition of CV3 chondritic meteorites [76]: 15% of the particles are 20 nm iron grain, while the remaining 85% are 25 nm silicate grains. Initial populations contain 2000 small aggregates of size $2 \leq N \leq 6$. The four sets of dust parameters analyzed, varying only for the iron grains within a population, are: 1) magnetized grains (M), 2) charged grains (Q), 3) both magnetization and charge on grains (MQ), and 4) no charge or magnetization, ballistic collisions (B).

The presence of charged iron grains and uncharged silicate grains may be attributed to the difference of the material dependent work functions, which is lower for iron. Due to the small radii of particles this difference produces a charge from photoemission equivalent to a single electron on iron monomers and no charge on silicate monomers for temperatures of $T < 270K$.

Grains were placed in a cube of space, with sides of 150 μm, giving a dust density on the order of $10^{-7} kg/m^3$. Typical dust densities in astrophysical environments typically range around $10^{-12} kg/m^3$. This artificially high density is used to reduce the overall computational time for the simulation. Artificially high densities do not alter the behavior of the populations of aggregates but simply allow for them to evolve on more computationally friendly time scales.

4.4.2 box_tree Aggregation

Each of the populations described in the previous section were allowed to evolve for equal time intervals and then compared to determine variations in coagulation behavior based on material properties. The magnitude of the charge as well as the electric and magnetic dipoles are compared for Populations Q and MQ, as well as

Populations M and MQ. The evolution of the dipole moment as aggregates grow to large size indicates the level of attractive electrostatic and magnetostatic interactions between particles. The morphology of each population is examined using the compactness factor. In addition to this physical parameter, the friction time for each population is compared to determine how well the aggregates remain entrained in their gas environment.

4.4.2.1 *Coagulation Rates.* Simulations of aggregates were allowed to evolve for equal periods of simulation time at the artificially high densities described. Tracking the number of aggregates in a simulation gives an indication of the rate of collisions based on the interparticle forces due to the material properties of each population. The number of aggregates in each population as a function of time is shown in Figure 4.8. Population B retains a larger number of aggregates by the end of the simulation compared to the other three populations due to the lack of interactions between particles. Population M begins has an initially rapid rate of coagulation that declines as fewer particles remain in the simulation to collide. Collisions between aggregates in population Q lag initially due to Coulomb repulsion, but then the total particle number rapidly decreases. The number of aggregates in population MQ as the simulation progresses is intermediate to the populations M and Q, as expected.

The drop in the number of aggregates for the charged population may be attributed to the rapid accumulation of smaller aggregates into the largest aggregates, as evidenced by the growth of the largest particle in the population shown in Figure 4.9. This may be explained by the difficulty for similar sized aggregates to collide due to Coulomb repulsion; only aggregates of differing sizes have great enough relative velocities to collide, therefore smaller particles are preferentially coagulated onto the largest particles. In contrast to population Q, populations M and MQ show a much smaller largest aggregate size. This indicates that smaller aggregates

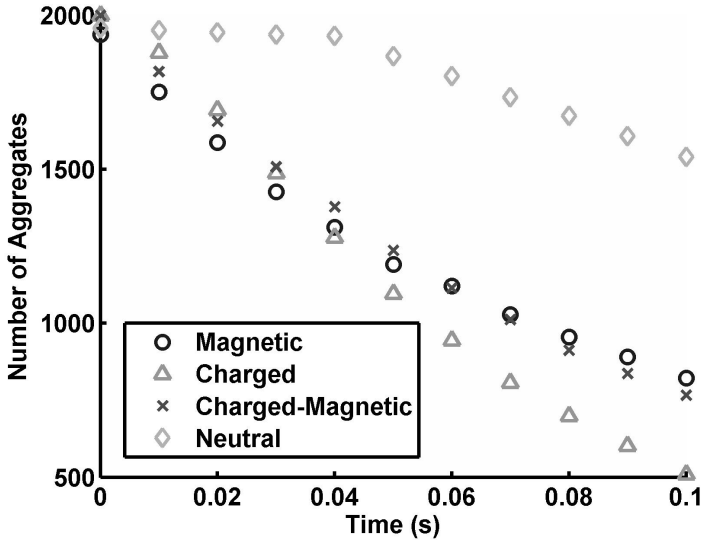

Figure 4.8: The number of aggregates within each population as the simulations progress. While the number of neutral aggregates decreases steadily over time, the populations which experience interparticle forces decrease in number more rapidly.

are swept up into a group of moderate sized aggregates, without runaway growth of a single aggregate. The largest aggregate in population MQ exhibits an interesting transition of behavior towards the end of the simulation: initially, the largest size aggregates in populations MQ and M are almost indentical, but as the simulation progresses the largest aggregate of MQ begins to grow more quickly, as does the largest particle from population Q.

4.4.2.2 *Dipole Moments.* The electric dipole moments for the charged and charged-magnetic populations are shown in Figure 4.10. In previous studies, it was found that although the dipole moment of charged grains does not vary strongly with size [69], it does vary with the morphology of the aggregate, the maximum moment of inertia. For charged particles, this trend can be seen here as well. Although the electric dipole of the MQ population depends weakly on size, the steeper slope, compared to the Q population, can be attributed to the fact that charged-magnetic aggregates are fluffier than charged aggregates indicated by the compactness factor.

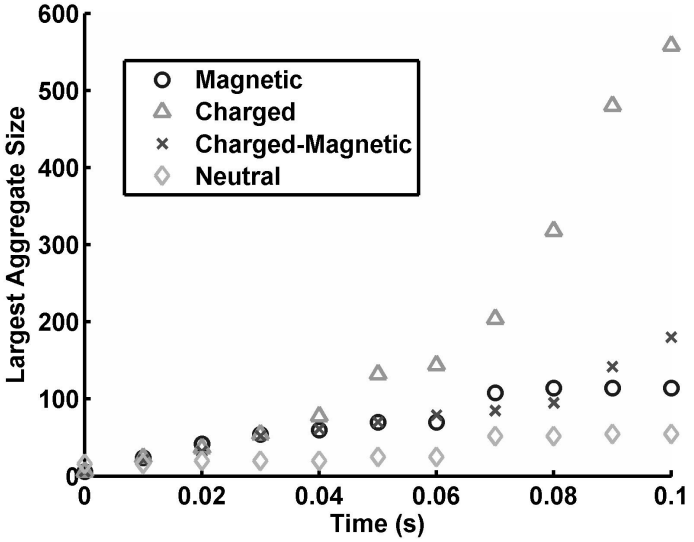

Figure 4.9: The size of the largest aggregates within each population as the simulation time moves forward. All populations are seen to have their largest aggregate grow slowly initially. Charged populations exhibit a very rapid accumulation of material upon the largest aggregate, termed run away growth. Magnetic and charged-magnetic populations appear to grow at a more sedate pace, though still more quickly than ballistic populations.

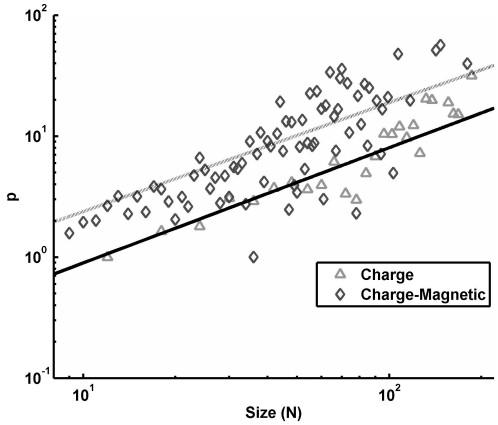

Figure 4.10: Electric dipole moment versus size. The fit lines for the two populations change according to $Q_q \propto I^{0.45}$ for charged aggregates and $Q_{\mu q} \propto I^{0.4762}$.

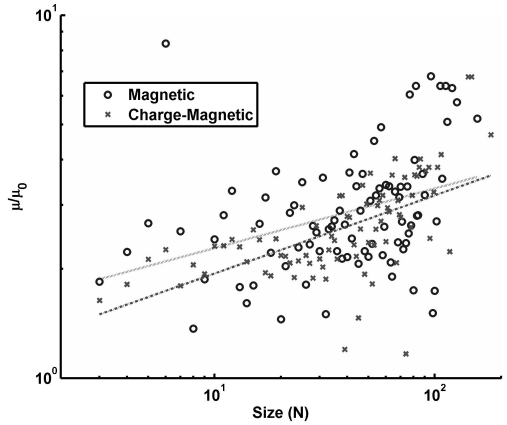

Figure 4.11: Normalilzed magnetic dipole moment versus size. The fit lines for the two populations change according to $\mu_\mu \propto N^{0.32}$ for magnetic aggregates and $\mu_{\mu q} \propto N^{0.42}$.

The comparison between magnetic dipoles for the M and the MQ populations is shown in Figure 4.11, where the magnetic dipole is taken to be a simple vector sum of the magnetic dipole of each ferromagnetic monomer within an aggregate. Even though the magnetic dipoles are similar in magnitude, the trends for the two populations differ. The ratio of the slopes for the exponential fits of the MQ to M populations is approximately 1.3. The larger rate of growth for the charged-magnetic population can be attributed to the increased time for alignment of the magnetic dipoles between colliding aggregates due to the reduced collisional speed from coulomb repulsion.

The magnetic dipole more strongly depends on size than does the charge dipole. This implies that as aggregates grow to large size the magnetic interactions may play an increasingly important role in the interaction between particles in a protoplanetary disk.

4.4.2.3 *Aggregate Morphologies.* Compactness factors calculated for both charged and magnetic populations are shown in Figure 4.12. As aggregates collide and grow to larger sizes, their compactness factors become lower, forming fluffy structures in the absence of restructuring. Aggregates containing only magnetic material are

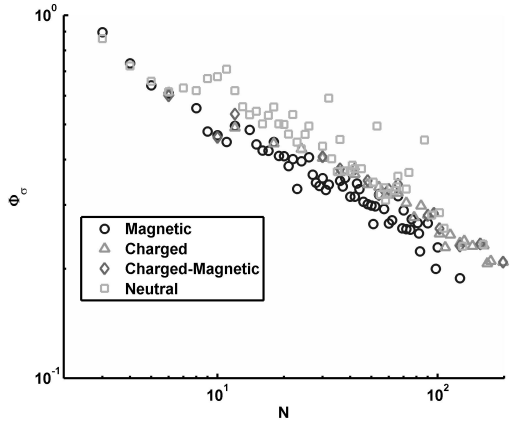

Figure 4.12. Average compactness factors versus size for all aggregate populations.

seen to have the lowest compactness factors throughout the evolution, corresponding to the most open structures with the largest geometric cross-section. Aggregates containing charged material are seen to have slightly higher compactness factors indicating denser and more compact structures. Aggregates containing material that is both charged and magnetic have compactness factors similar to those of charged particles at lower size but tend to more intermediate behavior compared to magnetic and charged aggregates as growth continues.

Aggregates built from magnetic material have lower compactness factors, Figure 4.12. Larger cross-sections allow aggregates to efficiently sweep up neighboring material, which results from the alignment of the magnetic dipoles during collision.

4.4.2.4 *Gas Response Times.* Friction times for each of the populations are shown in Figure 4.13. According to Eq 3.25, aggregates with a larger maximum radius should have lower friction times when compared to those of roughly equivalent mass. Populations M and MQ are seen to have lower friction times than population Q, especially at larger size, up to an order of magnitude. This is expected as aggregates grown under the influence of magnetic dipole interactions tend to be fluffier structures. The differences in friction time would yield altered relative velocities for

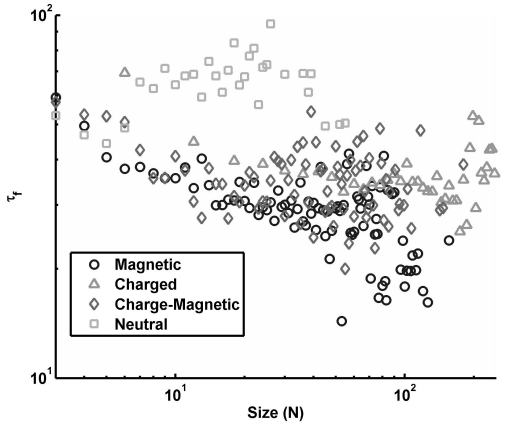

Figure 4.13. Evolution of average friction times versus size for all aggregate populations

different populations, changing the overall coagulation behavior. Population B aggregates have the highest friction times, in accordance with the compactness factor seen for such aggregates in the previous section.

Another implication of the fluffy, porous nature of the magnetic aggregates is that they remain better entrained in the gas environment than non-magnetic aggregates. This coupling to the gas will allow aggregates containing magnetic material to have smaller relative velocities to the gas compared to aggregates grown from ballistic or electrostatic collisions. This may lead to slower collisions with smaller energies present during coagulation.

4.5 Summary

Coagulation under the influence of both electrostatic and magnetostatic interactions has been examined using two numerical models; one which tracks pair-wise interactions and one which uses an N-body code. In both simulations magnetic interactions were seen to lead to aggregates which were fluffier in nature than those grown from charged or ballistic aggregation. When both charge and magnetization were included on monomers the behavior of aggregates were seen to be intermediate to the behavior seen from purely charged or magnetic populations. The rate of coagulation in large dust populations, from box_tree, was seen to favor the purely

electrostatic interactions, which were seen to experience runaway growth at later simulation times. This behavior is replicated much later by the charged-magnetic population but at a more sedate pace.

CHAPTER FIVE

Effect of Monomer Shape on Aggregate Morphology

Portions of this Chapter have been published as "The Influence of Monomer Shape on Aggregate Morphologies" *A&A* 539, 2012.

5.1 Motivation

Over the past decades there have been a multitude of numerical models employed to investigate the dynamics and properties of dust particles [42, 44, 45, 46, 73, 77]. One similarity between most of these models has been the near ubiquitous assumption of spherical monomers as the building blocks of aggregates. As presented in Section 1.4, however, there is a growing collection of evidence for the presence of non-spherical particle in environments where coagulation is common.

One recent study compared the aggregation of ellipsoidal and spherical monomers, using PCA and CCA aggregation methods. This study, performed by Bertini et al., concluded that the variation in morphology produced from differing monomer shapes was too small to influence the overall structure and porosity of the resulting aggregate structures [78]. Three different coagulation methods were employed to come to this conclusion: in the first population, PCA1, an incoming monomer had a trajectory directed towards the COM of a target particle; the second population, CCA, started with a small particle cluster of size $N = 2, 3$ or 7, replicated the cluster, rotated it to a new orientation and then collided it with a target, also using a trajectory directed towards the COM. The final population, PCA2, grew highly linear structures by using incoming trajectories vectored toward the closest monomer within the target particle.

The morphologies of the resulting aggregates were analyzed using porosity, fractal dimension, and friction time parameterized by the collisional cross section

of the particle. It was found that the porosity of aggregates consisting of spherical or ellipsoidal monomers varied by a small amount ($\sim$ 5%) between populations, which is even less than the differences seen among aggregates using polydisperse populations for the initial monomers. The variance found for fractal dimension was negligible, being $< 2\%$, and shape was concluded to not have an influence on this parameter. Finally, the friction time, depending on the inverse of the cross-section per unit mass, showed a difference of $\sim 15\%$ for the two aggregate types formed from CCA collisions, implying a stronger coupling to the gas for aggregates built using ellipsoidal monomers, even though this trend was concluded to be independent of the shape of the monomers. Overall the authors determined that shape was not an important factor in the aggregation process.

This study, however, lacked several parameters necessary to realistically model aggregation in an astrophysical environment. The following section reexamines the question of the effect of monomer shape on aggregation by incorporating two new parameters, including off-center collisions (impact parameter) and rotations of particles induced during collisions. It will be shown that although the results referenced are correct within the strict limitations of their assumptions, the inclusion of these parameters can have a large impact on aggregate structure. As such, their inclusion is necessary for accurate aggregation modeling.

5.2 Aggregation of Non-Spherical Particles

The model employed, *Aggregate Builder*, was modified to allow for ellipsoidal shapes by specifying three different axes for each monomer and tracking their orientations within the aggregate structure. The spheres and ellipsoids used in this study were of equal volume and mass. The ellipsoidal shape employed here is convex prolate with an aspect ratio of $3:1:1$, mirroring the shape used in the previous model [78]. The particles were assumed to be silicates (with density $\rho = 2.52\frac{kg}{m^3}$) with radii

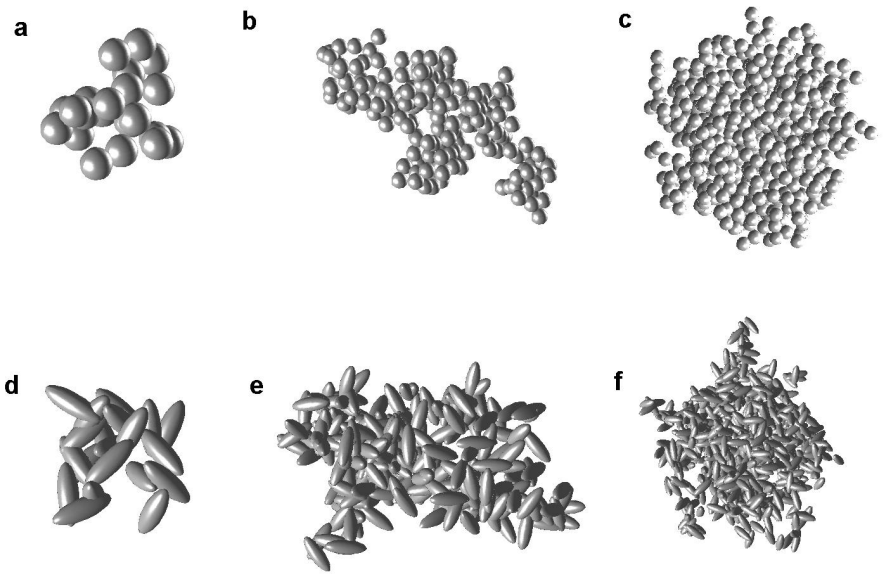

Figure 5.1: Sample aggregates generated from the model described in the text a) PCA aggregate built from spheres (N = 20), b) CCA aggregate built from spheres (N $\sim$ 200), c) PCA aggregate built from spheres (N $\sim$ 700), d) PCA aggregate built from ellipsoids (N = 20), e) CCA aggregate built from ellipsoids (N $\sim$ 200), f) PCA aggregate built from ellipsoids (N $\sim$ 700).

of $R = 2.88\ \mu m$ for spherical monomers and $R = 6\ \mu m$ for the semi-major axis of the ellipsoidal monomers.

5.2.1 Aggregate Morphologies

Sample aggregates grown using the PCA and CCA mechanisms are shown in Figure 5.1. The differences in the morphology of the aggregates and between populations is presented in detail below. Raw data sets for the physical quantities exhibited have been binned according to aggregate size, N, and averaged for clarity in examining trends as particles grow to large size. Due to the differing trends in the morphologies between aggregation regimes, PCA and CCA results shall be discussed separately.

In Figures 5.2a-b, dashed lines indicate the results from collisions assuming no rotation or off-center collisions, essentially a replication of the Bertini et al. results. A difference in two populations is seen when rotations (induced by off-center collisions) are incorporated in the parameter space as indicated by the data points with their associated error bars. When rotations are not allowed, including an impact parameter, b, does not alter the previously reported results, since an off-center impact is equivalent to an impact directed toward the COM along a different approach vector during ballistic collisions. Thus, the difference in physical characteristics for aggregation consisting of two monomer types is due primarily to induced rotation.

The aggregate spin rates, shown in Figure 5.3, indicate that the mechanical spin rate of the aggregates evolves similarly for both shapes, as would be expected for aggregates grown through impacts between particles of equal mass and speed. The magnitudes of the induced rotations differ by $\sim$ 10% for PCA collisions and $\sim$ 5% for CCA collisions. These differences are not large enough to produce the additional structural variations seen in Figures 5.4-5.5. This is in agreement with Paszun and Dominik, within assumed limitations, who also found that rotations play a significant role in determining the structure of aggregates [79]. In their work, Brownian rotations led to the formation of elongated aggregates, especially in the non-ballistic limit of dense gaseous environments.

5.2.1.1 *Cluster-Cluster Aggregation.* As shown in Figure 5.2a, aggregates built from ellipsoids tend to be less porous than aggregates built from spheres for CCA collisions, and have a greater variation at any given size. The average difference in porosity for CCA populations to almost 15%. For comparison purposes, the dashed lines in Figure 5.2a indicate the porosity of aggregates grown without the inclusion of offsets or rotations during potential collisions. For this case, the results for ellipsoids and spheres overlap almost exactly, in agreement with Bertini et al.,

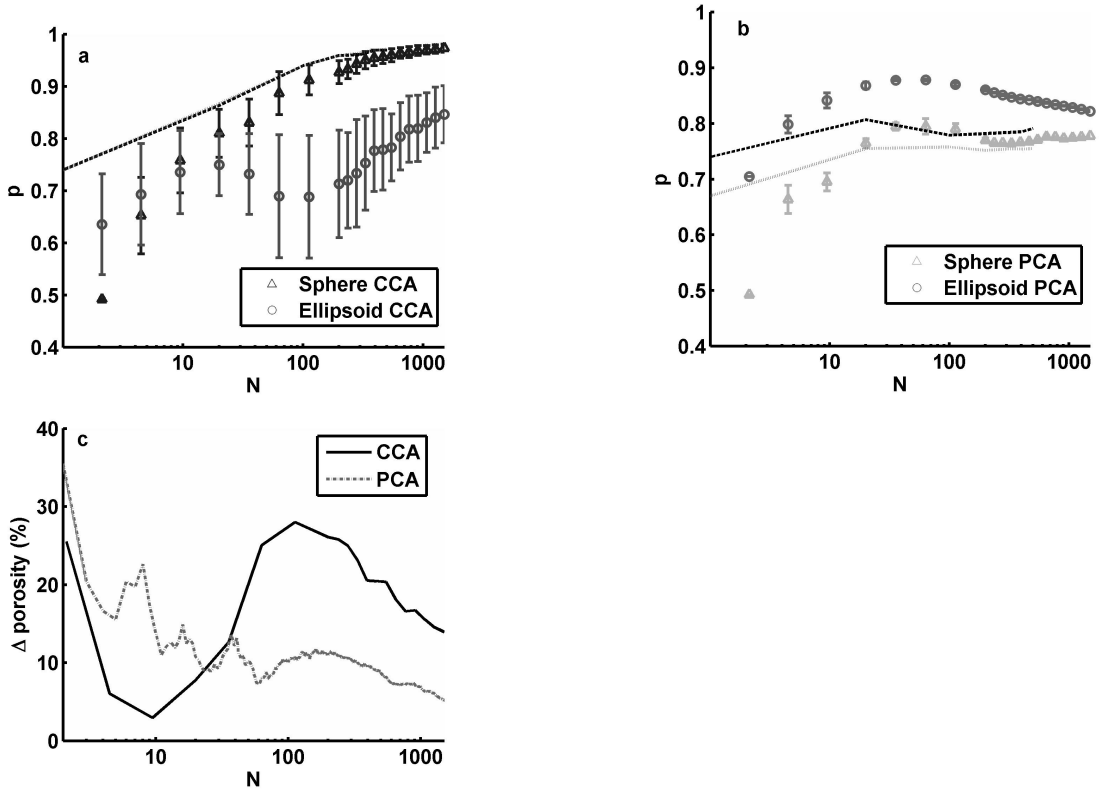

Figure 5.2: Average porosities for a) populations built from CCA collisions, and b) populations built from PCA collisions. c) Percent difference between aggregates built using different monomer shapes within the same collision regime. The lines in a) and b) represent the porosities of populations grown without using an offset or rotation replicating the results of Bertini et al. [78]. The darker line corresponds to aggregates comprised of ellipsoidal monomers, while the lighter is for aggregates comprised of spherical monomers. In a) the differences between spheres and ellipsoids are so small that the trend lines coincide at all points.

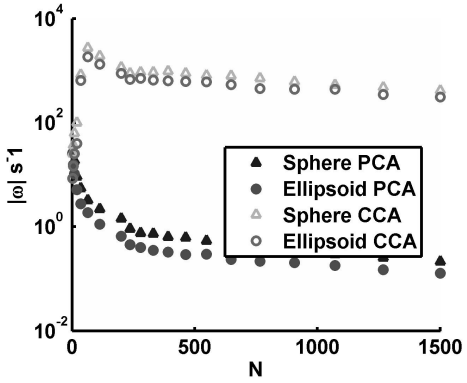

Figure 5.3: Magnitude of rotations induced by off-center collisions during the aggregation process. Collisions between clusters are seen to produce much higher spin rates than collisions of a single particle with a cluster, as expected.

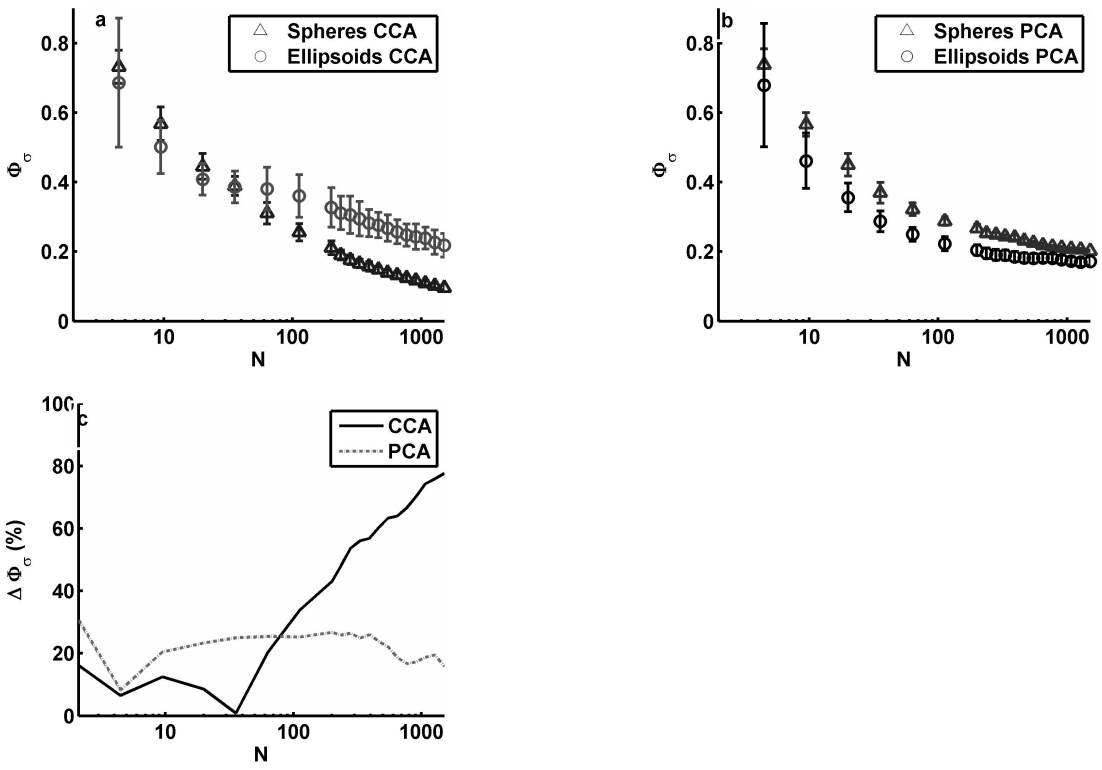

Figure 5.4: Average compactness factor (with associated errors) for a) populations built using CCA collisions, and b) populations built using PCA collisions. c) Percent difference between aggregates built using different monomer shapes in the same collision regime.

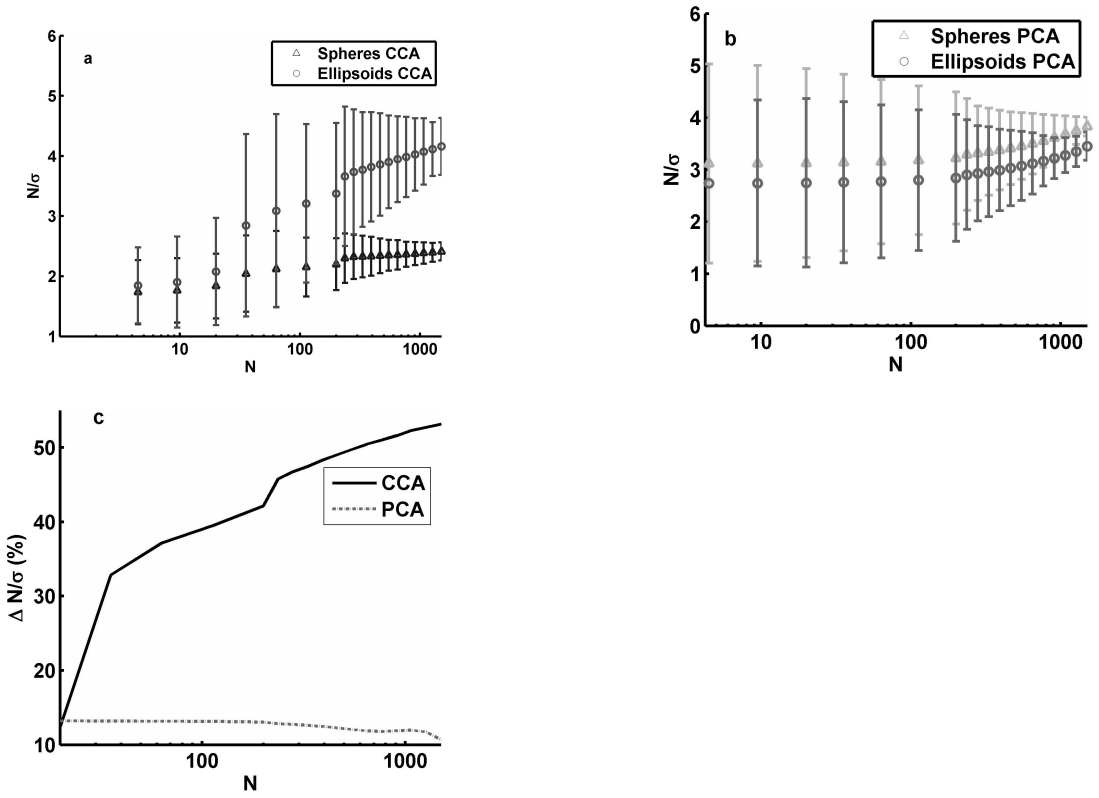

Figure 5.5: Average friction times (with associated errors) calculated using a normalized geometric cross-section and for arbitrary environmental parameters for a) populations built using CCA collisions, and b) populations built using PCA collisions. c) Percent different between aggregates built using different monomer shapes in the same collision regime.

where the average percent difference between the two populations was essentially null [78].

The compactness factor, as calculated by Equation 3.21 and shown in Figure 5.4, indicates that aggregates comprised of spheres are much less compact than those grown using ellipsoids, in agreement with the trend for porosity. While the difference is relatively minor for small aggregates, $N \leq 20$, the difference becomes greater as aggregates grow to large size (Figure 5.4c). Additionally, the standard deviation is larger for ellipsoids than for spheres, implying a broader variation in structure for those aggregates.

The evolution of friction times, for the shapes used in this study, differe substantially as aggregates grow to larger sizes, Figure 5.5a. The friction times for aggregates built from spheres increase only slightly with size, while those comprised of ellipsoids have significantly larger friction time for aggregates with size $N > 20$. This leads to a significant difference between aggregates formed from spheres and ellipsoids for all but the smallest aggregates (Figure 5.5c), ellipsoidal aggregates more than doubling their response time as they grow. Coupled with the larger deviation seen in friction times across all sizes, this implies that turbulence could be a very effective mechanism for producing relative velocities which lead to coagulation for ellipsoidal particles.

5.2.1.2 *Particle-Cluster Aggregation.* In contrast to the CCA regime, PCA aggregation of ellipsoids generates aggregates that are more porous than aggregates consisting of spheres (Figure 5.2b). In this case, the variance for a given size is quite small for both monomer shapes. The overall differences in the porosity of the two populations is $\sim 9\%$, decreasing for larger aggregates. The dashed lines in Figure 5.Xb again represent the resulting porosity when rotations induced by offset collisions are not incorporated into the model. In this case, the difference for the

two populations is about 4% (Figure 5.2c), in agreement with Bertini et al., who, found a difference of $\sim 5\%$.

The compactness factors for PCA aggregates tend to a similar limiting value for large N (Figure 5.4b). This leads to a smaller, but not insignificant, difference between the compactness of these structures as exhibited in Figure 5.4c. While the variance within both populations in comparatively small, aggregates built with ellipsoids still exhibit a larger range of compactness factors for a given size.

Also in contrast to the CCA regime, the number of monomers per geometric cross-section, $\frac{N}{\sigma}$, and thus the friction times, of PCA aggregates evolve almost identically during growth (Figure 5.5b). Populations also exhibit similar variance at all sizes. This leads to a difference between the populations which, while being more modest, is not negligible, averaging $\sim 12\%$ for all sizes (Figure 5.5c).

5.2.2 Implications

Populations of aggregates consisting of either spherical or prolate ellipsoidal monomers grown using both PCA and CCA methods were compared according to porosity, compactness factor and friction time. Inclusion of an impact parameter and rotational degrees of freedom, neglected in previous work, created aggregates with large structural differences. Differences between the two populations is always smaller for PCA, ranging between $10 - 20\%$ for structural characteristics such as porosity and compactness factor. For CCA aggregation, however, the differences exhibited in compactness factor and friction times are significant as aggregates grow to larger size (up to 50%), and can have a large impact on the evolution of a protoplanetary disk or a molecular dust cloud.

These results illustrate the importance of considering the rotation of particles in astrophysical systems. Rotations may be caused by the conservation of angular momentum, as used in this model, or from Brownian rotation, which may play

a significant role in dense gaseous environments [79]. Thus far only a single size of monomer was examined, a monodisperse population. Realistically, individual particles in dusty environments will be distributed over some range of possible sizes. Additionally, only a single alternative to the simple symmetric spherical structure was examined. The next section expands upon both of these limitations as a full examination of ballistic collision of non-spherical monomers.

5.3 Polydisperse Monomer Populations

Sizes of dust grains within physically relevant populations are unlikely to exist at a single fixed monomer size. It is therefore useful to examine the morphological progression of aggregates under polydisperse monomer distributions for ballistic collisions. To accomplish this, *Aggregate Builder* was modified to permit the monomer axes to be set to any desired aspect ratio, allowing various ellipsoidal shapes to be examined. The monomer distribution was also modified to follow an exponential size distribution characterized by

$$n(r) = r^{-\alpha} dr \tag{5.1}$$

where r is the semi-major axis (or radius) of a monomer and α is an exponent which determined the slope of the size distribution [5].

Three monomer shapes were selected for study using polydisperse monomer distributions. Spherical monomers were initially employed to establish control populations for comparison. Next, prolate ellipsoidal monomers (with one semi-major axis and two equal semi-minor axes) and oblate ellipsoidal monomers (with two equal semi-major axes and one semi-minor axis) were examined. The maximum and minimum radii used in each separate model were varied to maintain a constant volume and mass for monomers. Monomer shapes, aspect ratios and radii (semi-major axes) for all populations are shown in Table 5.1.

Table 5.1: Aspect ratio and sizes for monomer shapes used to grow aggregates through ballistic collisions. Min/max sizes for each monomer shape correspond to equal volumes.

Monomer Shape	Aspect Ratio	Radii μm
Spherical	1:1:1	0.120 - 2.404
	3:1:1	0.250 - 5.000
Prolate Ellipsoidal	5:1:1	0.351-7.029
	10:1:1	0.558-11.16
	3:3:1	0.173-3.460
Oblate Ellipsoidal	5:5:1	0.206-4.110
	10:10:1	0.259-5.179

Two representative values of α, $\alpha = 1.8$ and 3.5, were used in this study. Observations of the interstellar medium (ISM) in the near- and mid-infrared (IR) ranges have suggested dust size distributions as low as $\alpha = 1.8$, while observations taken in the ultraviolet (UV) and visible spectrum suggest size distributions having exponents as large as $\alpha = 3.5$ [80, 81]. Monodisperse populations, i.e. $\alpha = \infty$, were also modeled for the smallest and largest possible monomer sizes for each shape tested.

5.3.1 Analysis of Polydisperse Aggregation

A representative sampling of aggregates grown assuming ballistic collisions under the conditions described in the previous section is shown in Figure 5.6. The results presented within this section represent averages for the parameters binned by mass and normalized by the minimum monomer mass, m/m_0, or number of monomers , N. Under the ballistic aggregation regime employed, the two monodisperse populations were found to have nearly equivalent values for the characteristic examined, so for clarity only the resulting data from the larger monodisperse population is presented in Figures 5.7-5.12.

The radius of the average geometric cross-section, R_σ, grows via a power law, $(R_\sigma \propto (\frac{m}{m_0}^\beta))$, defined in Section 3.5.4, as shown in Figure 5.7. Here R_σ has been nor-

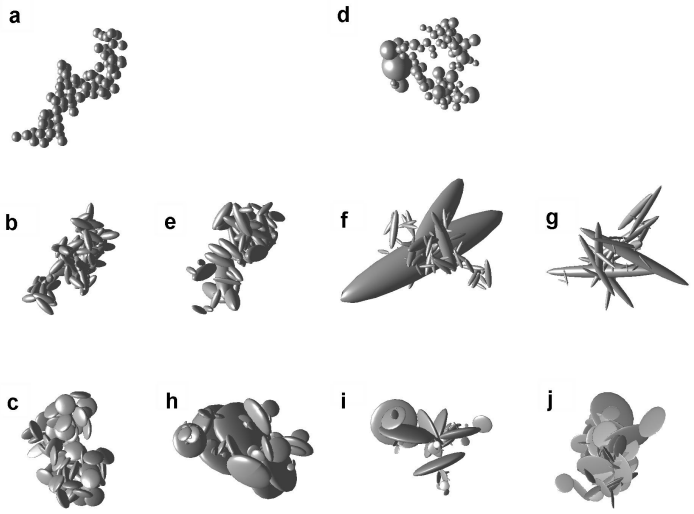

Figure 5.6: Sample aggregates grown from populations using the method described in Section 2. Each aggregate contains ≈ 80 monomers using a-c) monodisperse spheres, prolate ellipsoids (3:1:1), and oblate ellipsoids (3:3:1), d) polydisperse spheres, e-g) polydisperse prolate ellipsoids with axis ratios (3:1:1), (5:1:1), and (10:1:1) respectively, and h-j) polydisperse oblate ellipsoids with axis ratios (3:3:1), (5:5:1), and (10:10:1) respectively.

malized by the smallest average monomer radius for each population. Independent of the monomer sizes and distributions, aggregates comprised of spherical monomers, on average, have a radius which grows faster with mass than do aggregates comprised of either type of ellipsoidal monomers, as measured by the slope of the fit line to the data. The simplest reason for this is that ellipsoidal shapes can pack more efficiently than spheres, as is also reflected in the larger compactness factors seen for ellipsoids, shown hereafter.

Comparing aggregates composed of ellipsoidal monomers, it is seen that prolate and oblate shapes having the same aspect ratio both form aggregates which grow via the same power law exponent. It is interesting to note that the exponent does not vary much as the aspect ratio is increased, and that the monodisperse and power law distributions may be fit by the same trend line. The largest deviations from this single fit line at large sizes are seen for spheres; on the other hand, small aggregates

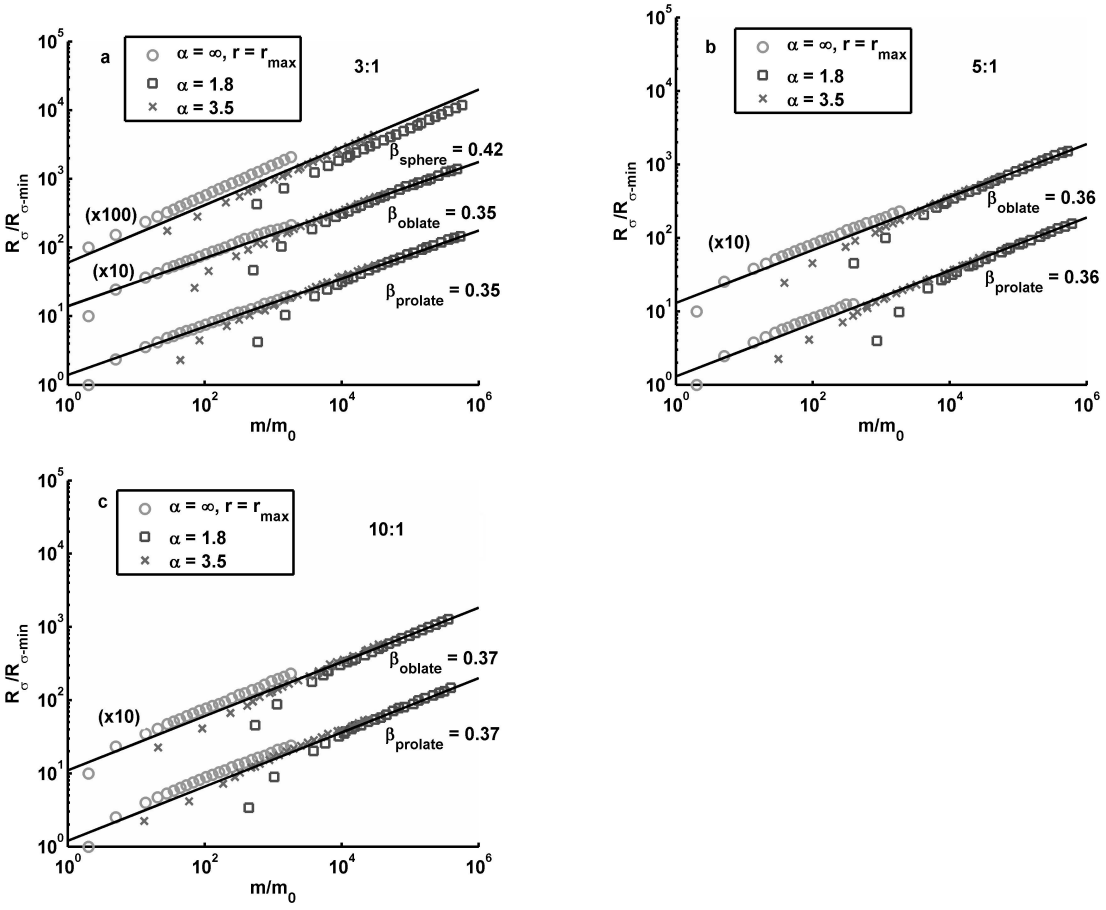

Figure 5.7: Average R_σ versus mass built from the larger monodisperse population and two different polydisperse populations. The solid line shows the trend for the combined populations for each monomer shape with the slope, β, indicated for a) two types of ellipsoids with aspect ratios of $(3:1)$, compared to spheres, b) ellipsoids with aspect rations of $(5:1)$, and c) ellipsoids with aspect ratios of $(10:1)$. For clarity oblate and spherical populations have been offset by x10 and x100 respectively.

consisting of polydisperse monomers have large deviations from the fit line which has interesting consequences for the friction times, shown later.

An indication of the impact of the shape of dust monomers in the difference is the morphologies of the resulting aggregates, characterized by the compactness factor shown as a function of mass in Figure 5.8 and as a function of N in Figure 5.9.

Aggregates constructed from spheres (Figure 5.8a) exhibit similar trends for all values of α, starting as very compact structures and smoothly approaching com-

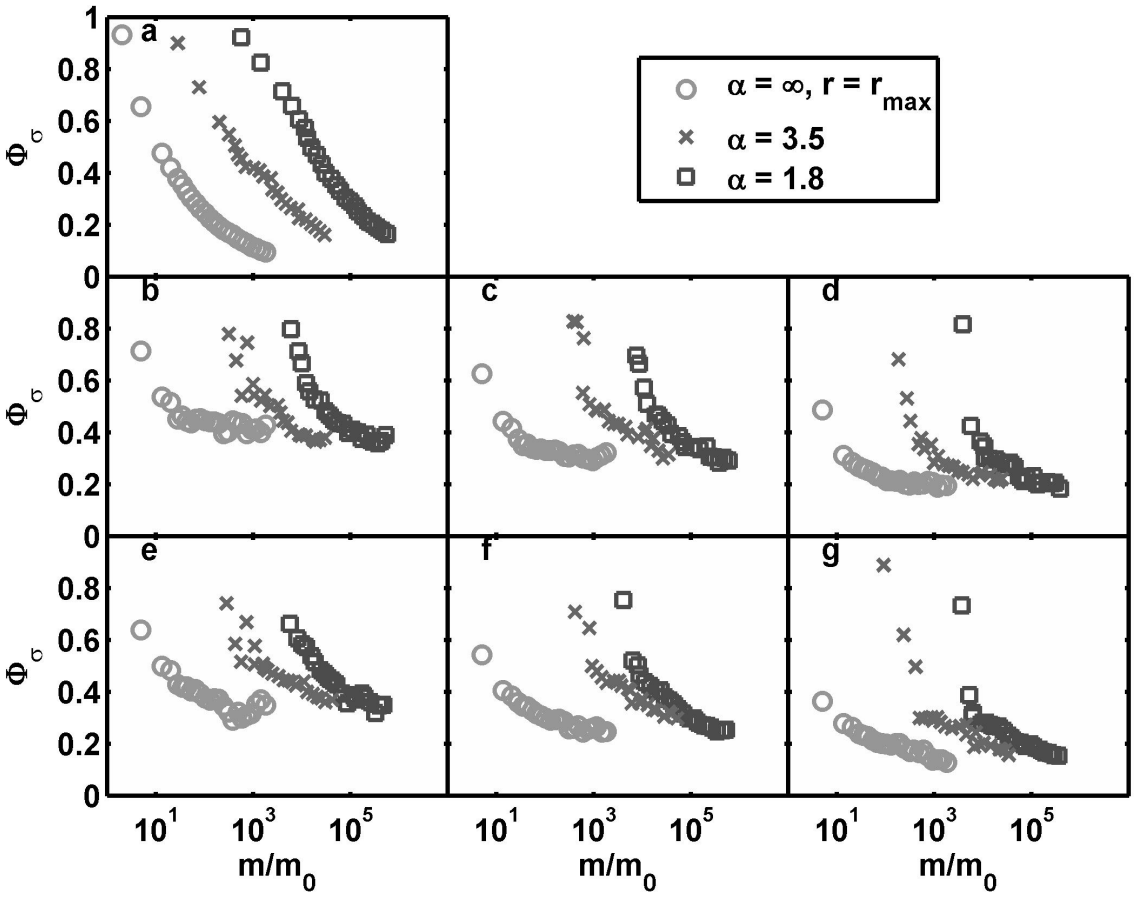

Figure 5.8: Average compactness factors versus normalized mass for aggregates built from the larger monodisperse population and two different polydisperse populations for a) spherical monomers, b-d) ellipsoidal prolate monomers with aspect ratios of $(3:1:1), (5:1:1)$, and $(10:1:1)$ respectively, and e-g) ellipsoidal oblate monomers with aspect ratios of $(3:3:1), (5:5:1)$, and $(10:10:1)$ respectively.

pactness factors of less than 0.2 (open, fluffy structures) as they grow larger. While aggregates composed of ellipsoidal monomers initially are less compact at small sizes, they rapidly approach a minimum limiting value for the compactness factor, which is higher than that found for spheres. The limiting value is essentially independent of the monomer distribution within the population, but does depend on the aspect ratio of the monomers. The limiting compactness factor for aggregates built from monomers with aspect rations of $3:1$ is ≈ 0.4 (Figures 5.8b and 5.8e, ≈ 0.3 for aspect ratios of $5:1$ (Figures 5.8c and 5.8f), and ≈ 0.2 for aspect ratios of $10:1$ (Figures 5.8d and 5.8g).

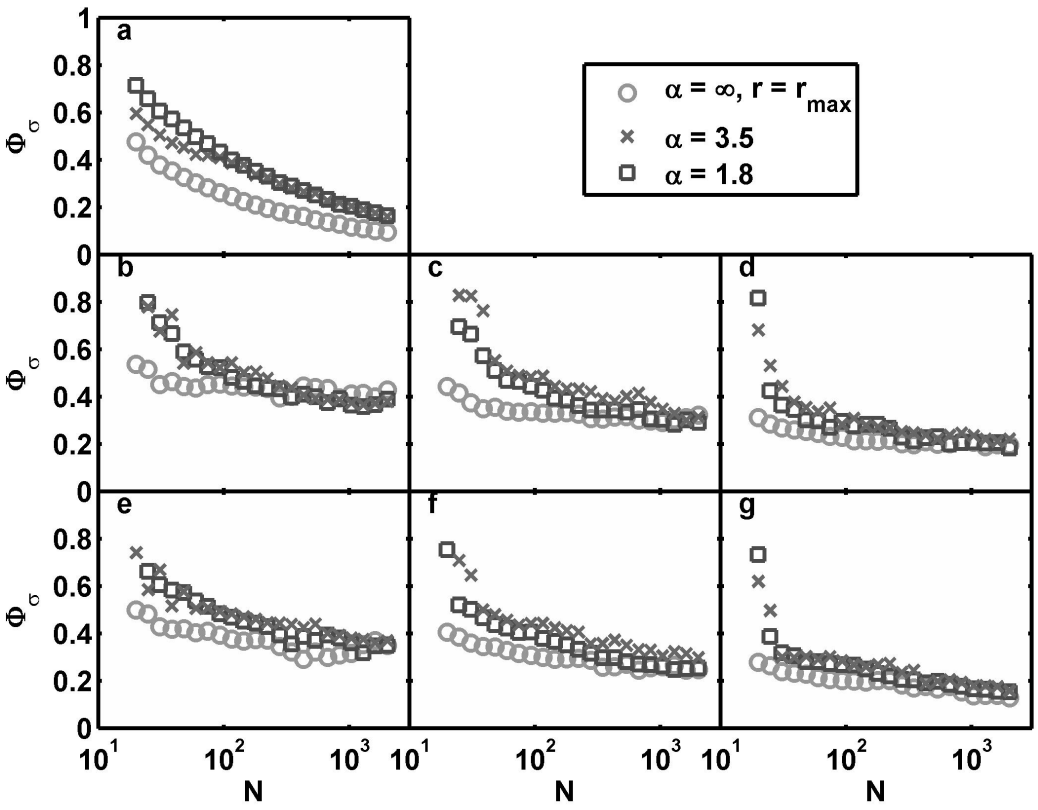

Figure 5.9: Average compactness factors versus number of monomers for second and third generation aggregates for a) spherical monomers, b-d) ellipsoidal prolate monomers with aspect ratios of $(3:1:1), (5:1:1)$, and $(10:1:1)$ respectively, and e-g) ellipsoidal oblate monomers with aspect ratios of $(3:3:1), (5:5:1)$, and $(10:10:1)$ respectively.

Examining the compactness factor as a function of N provides additional insight into aggregate growth. Data for second and third generation aggregates ($20 \leq N < 2000$) are shown in Figure 5.9. The trends for the polydisperse spheres are almost identical at large N, and the aggregates tend to be more compact than those built from monodisperse spheres, as can be seen in Figure 5.Xa. For ellipsoidal grains, the monodisperse populations are initially fluffier at small sizes, but quickly reach a minimum compactness factor, while the polydisperse aggregates approach the limiting value more slowly (Figures 5.9b-g). At large N, aggregates built from monodisperse and polydisperse monomer populations tend to have similar compactness factors, though the monodisperse populations are slightly fluffier for prolate ellipsoids $(3:1:1)$, Figure 5.9b.

Additional information on the evolution of the morphology of aggregates may be gleaned from the compactness factor by examining the standard deviations from the mean values, which were omitted from Figures 5.8 and 5.9 for the sake of clarity. Scaled standard deviation, $\sigma/\bar{\Phi}_\sigma$, versus scaled mass has been plotted in Figure 5.X for both monodisperse and polydisperse populations. Here a clear difference can be seen between aggregates built from spheres and ellipsoids. Spherical monomers tend to build self-similar aggregates, with small deviations from the mean compactness factor (on the order of 5%). Ellipsoidal monomers, on the other hand, build aggregates of a given mass with large differences in the compactness factors. The deviation from the mean is similar for all three of the aspect ratios. Monodisperse spheres lead to aggregates with a much smaller deviation in Φ_σ than do all sizes of monodisperse ellipsoids, Figure 5.10a. Polydisperse populations (Figures 5.10b and 5.10c) have comparable deviations initially, at the smallest aggregate sizes, but aggregates built from spheres exhibit a swiftly declining deviation, while ellipsoidal grains maintain a more constant or even slightly increasing deviation. For ellipsoids, all aspect ratios selected for this study tend to deviations of $\sigma/\bar{\Phi}_\sigma = 0.1 - 0.3$.

Friction times, normalized by the minimum monomer response time, τ_{min} within a given population, as a function of normalized mass, are shown in Figure 5.11. Aggregates built from spherical monomers have friction times which vary minimally as aggregates increase in size, Figure 5.11a. By comparison, aggregates built from ellipsoidal monomers have higher friction times which increase with size at a faster rate for all cases. From the graphs it is seen that the trends for friction times vary most strongly with the aspect ratio of the monomers themselves, not simply the monomer shape. For aspect ratios of $3:1$ the friction times have the steepest slope for larger aggregates; they also produce the most pronounced "bowl -shaped" minimum for mid-sized aggregates formed from polydisperse populations, Figures 5.11b and 5.11e. Aggregates built from monomers with aspect ratios of $5:1$

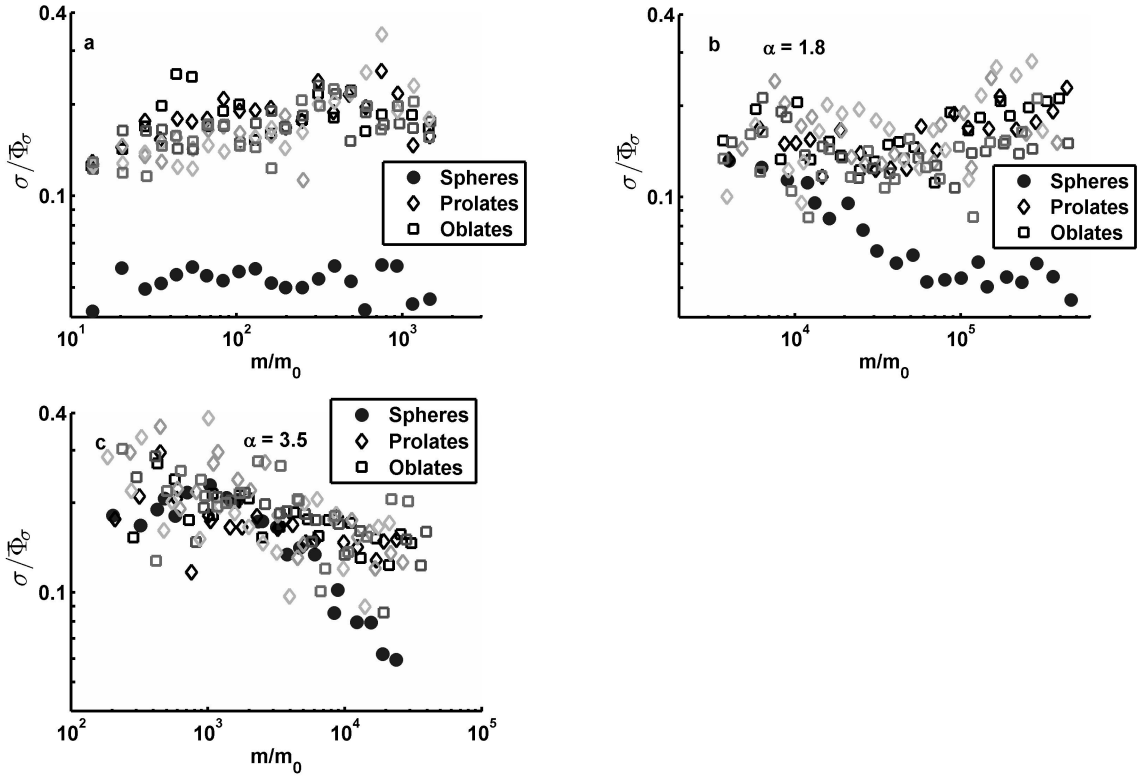

Figure 5.10: Standard deviations scaled by the average compactness factor versus scaled masses for a) monodisperse populations, b) polydisperse populations with $\alpha = 1.8$, and c) polydisperse populations with $\alpha = 3.5$. For the prolate and oblate populations, the black markers correspond to aspect ratios of $3:1$, the medium gray corresponds to aspect ratios of $5:1$, while the lightest gray denotes aspect ratios of $10:1$.

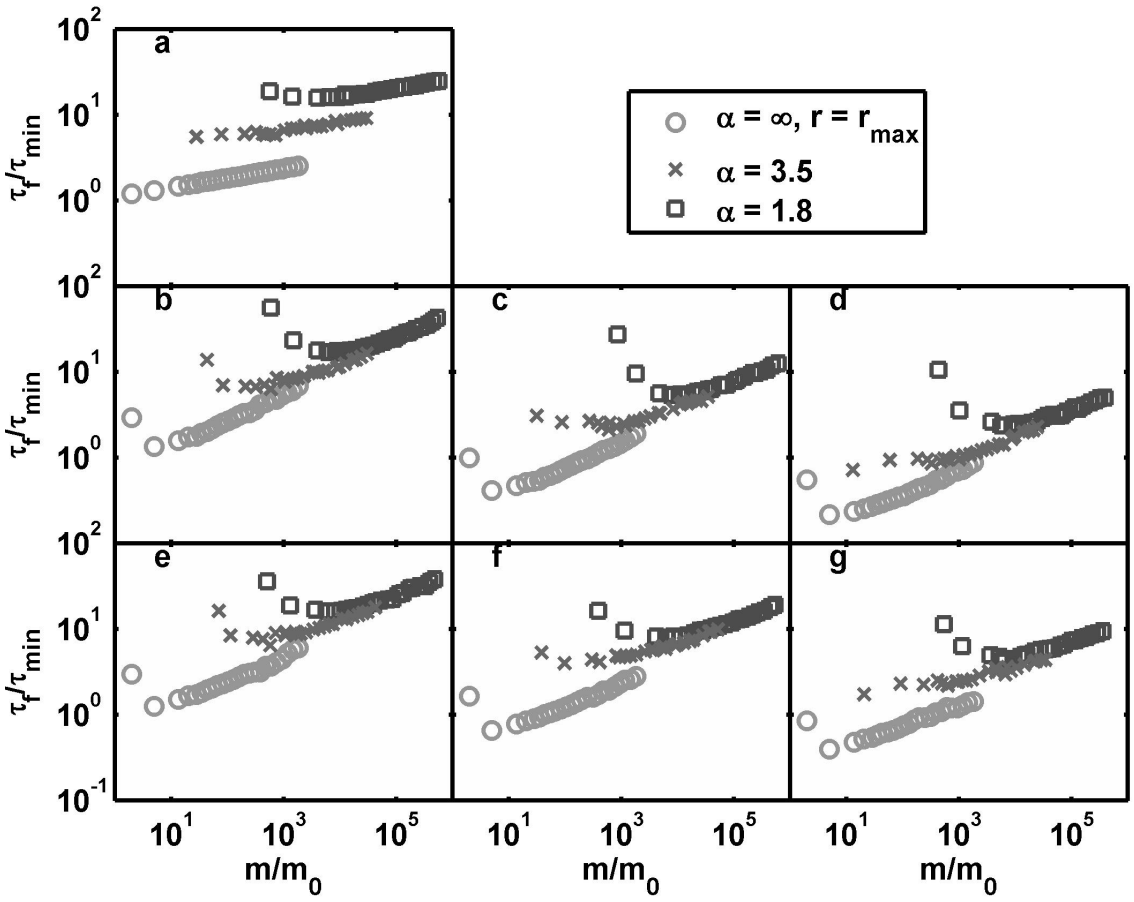

Figure 5.11: Normalized friction times versus normalized mass for aggregates built from the larger monodisperse population and two different polydisperse populations for a) spherical monomers, b-d) ellipsoidal prolate monomers with aspect ratios of $(3:1:1), (5:1:1)$, and $(10:1:1)$ respectively, and e-g) ellipsoidal oblate monomers with aspect ratios of $(3:3:1), (5:5:1)$, and $(10:10:1)$ respectively.

(Figures 5.11c and 5.11f) or 10 : 1 (Figures 5.11d and 5.11g), have friction times which increase more slowly with a shallower "bowl", especially as α increases.

Further details about the response of aggregates to their environment may be seen by examining the standard deviation from the mean friction times, which were omitted from the previous figure for clarity. Scaled standard deviation, $\sigma/\bar{\tau}_f$, versus normalized mass is shown in Figure 5.12 for both monodisperse and polydisperse populations. For monodisperse populations, Figure 5.12a, aggregates built from spheres show a much lower deviation than all ellipsoidal monomer populations, which all have very similar deviations. The standard deviation for polydisperse populations

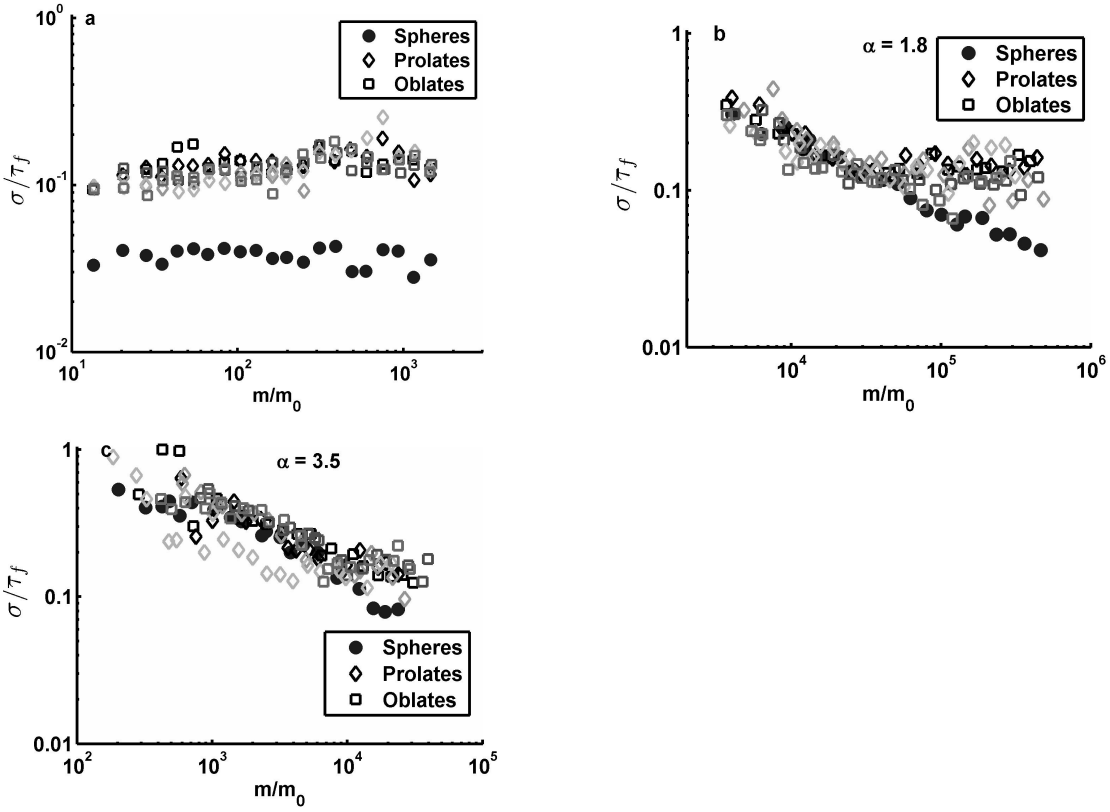

Figure 5.12: Standard deviations scaled by the average friction time versus normalized mass for a) monodisperse populations, b) polydisperse populations with $\alpha = 1.8$, and c) polydisperse populations with $\alpha = 3.5$. For the prolate and oblate populations, the black markers correspond to aspect ratios of $3:1$, the medium gray to aspect ratios of $5:1$, while the lightest gray denotes aspect ratios of $10:1$.

tends to decrease with aggregate size. Thus, aggregates composed of ellipsoidal monomers will typically have a broader range of friction times, especially at large sizes, producing a wider possible response to turbulence leading to varying relative velocities and enhanced collision probabilities.

5.3.2 Implications

Deviation from the standard assumption of spherical monomers for modeling dust coagulation was shown to have a definitive impact on the overall aggregate structure (characterized by the compactness factor) and the relative velocities (characterized by the friction time) for aggregates in astrophysical environments. It has

been shown that ellipsoidal monomers form aggregates which are more compact (less fluffy), have smaller equivalent radii, and exhibit a wider range of responses to turbulent eddies than do aggregates grown from spherical monomers.

Given these differences, the wide variation in structure and friction times seen for aggregates of a given size built from ellipsoids may make coagulation more efficient, as large aggregates can still have relatively large relative velocities with each other, driving collisions. Large aggregates built from spheres tend to have similar friction times, which leads to small relative velocities, eventually halting aggregate growth.

Finally, when comparing the possible deviations from spherical symmetry presented in this section, prolate and oblate ellipsoids, it appears that the type of deviation has a small impact on the physical parameters of resulting aggregates. Both ellipsoidal monomer types were seen to consistently yield similar results for the compactness factor, equivalent geometric radii, and friction times. This implies that the specific type of deviation from spherical symmetry (whether prolate or oblate) is a minor consideration. The major impact comes from the deviation from spherical particles and the aspect ratio, not the specific shape modeled.

5.4 Aggregation of Charged Ellipsoids

Aggregates were built using polydisperse monomer distributions, such as was described in the beginning of Section 5.3, assuming silicate grains, which have a density of $\rho = 2.54 \times 10^3\ kg/m^3$. Charging was assumed to be driven by solar radiation with ion and electron temperatures of $T_e = T_i = 4357K$. Collisions were driven by turbulent relative velocities, following the method presented in 2.1.4.

5.4.1 Charge Arrangement

During collisions between dust particles the charging algorithm OML_LOS is employed to recalculate and distribute charges on the aggregates and monomers re-

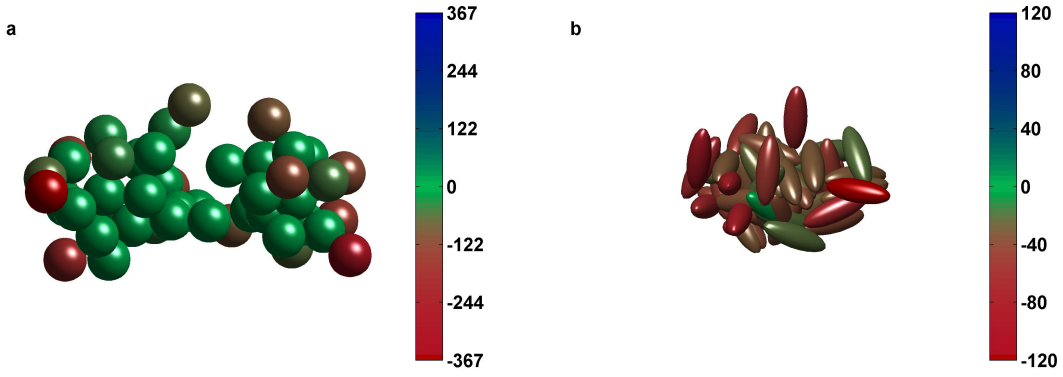

Figure 5.13: Charge mapping of aggregates built from a) $N = 48$ spherical monomers and b) $N = 64$ prolate ellipsoidal monomers. Colors correspond to the charge on each monomer in units of elementary charge.

spectively. The arrangement of charges on two representative aggregates is shown in Figure 5.13. For aggregates built from spherical monomers the bulk of the charges are found on the most exterior monomers, while the monomers closest to the COM have a very minimal charge, near neutrality. Aggregates which are composed of ellipsoidal monomers exhibit a more distributed charge arrangement over its geometry. Once again the most exterior monomers have the highest charges but the magnitude of this charge is reduced compared to the outer spherical monomers in an aggregate of similar size. At the same time, monomers closer to the COM have a larger charge than the interior spherical monomers. The cause for this difference in arrangement of charges is due to the difference in surface area, and the subsequent effects on the calculated LOS factor of ellipsoidal grains versus spherical grains.

The evolution of the charge on aggregates comprised of ellipsoids versus size is shown in Figure 5.14. The charge has been normalized by the charge on a single monomer in the model. As aggregates grow to larger size the total charge on the aggregate is seen to grow at a slow pace, changing at a rate similar to previous studies [73]. Most of the aggregate charges fall along the fit line, which obeys the relation of $Q = 0.8N^{0.42}Q_0$. However some charges are seen to deviate significantly

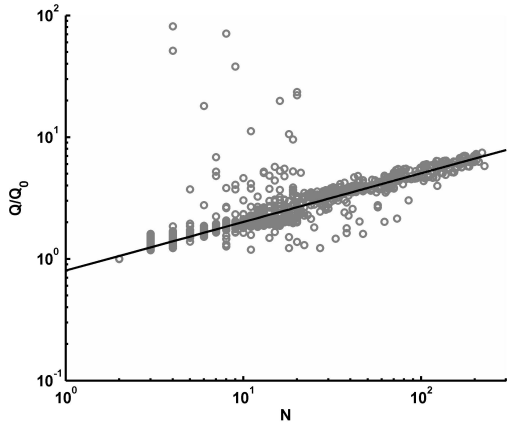

Figure 5.14: Normalized charge of aggregates constructed from ellipsoidal monomers versus size.

from this value. This is likely due to a large open LOS factor for the monomers within these aggregates, which is more easily obtained with ellipsoidal aggregates due to the large structural variaton of such aggregates.

5.4.2 Post-Coagulation Structure

The compactness factors of charged aggregates built from spheres and ellipsoids, subjected to the plasma conditions described in the beginning of this section, are shown in Figure 5.15. Aggregates built from spheres show a sharp decline in compactness factor at small size, indicating the growth of open, fluffy aggregates. This is in agreement with the structures observed resulting from charged aggregation in previous studies [73]. The compactness factors of aggregates built from spherical monomers tends to a limiting value of $\Phi_\sigma \approx 0.2$.

Aggregates built from the prolate ellipsoidal monomers employed exhibit a more gradual decrease in compactness factor. With the exception of small cluster sizes, aggregates built from ellipsoids are always more compact, and therefore more dense, at all sizes. These aggregates tend to a limiting value of $\Phi_\sigma \approx 0.4$. This more compact nature for aggregates is due to a mixture of the packing efficiency of the ellipsoidal shape as well as the reduced magnitude of the most exterior charges,

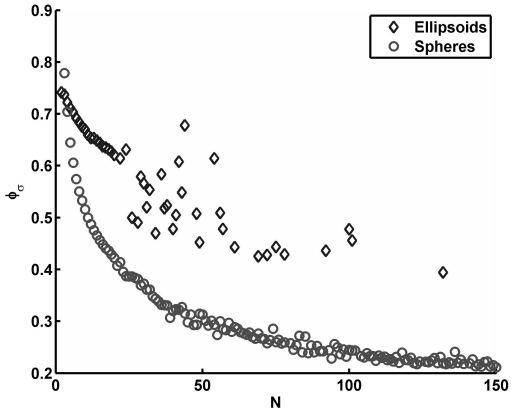

Figure 5.15: The compactness factors of charged aggregates composed of charged particles (ellipsoids or spheres) versus size (N).

permitting more frequent collisions between interior monomers. Higher exterior charges increase the Coulomb repulsion, which cause collisions between external monomers from induced rotations.

CHAPTER SIX

Conclusions and Future Work

Numerical simulations of the coagulation of dust particles incorporating various dust parameters has been presented. Two different effects have been examined: electromagnetic interactions between aggregates consisting of spherical monomers and the effect of non-spherical monomers on coagulation. The effect of electromagnetic interparticle forces have been examined by considering the effects of charge and magnetization separately and together, and comparing the results with coagulation from ballistic collisions (no interparticle forces). The coagulation of non-spherical monomers was modeled using both monodisperse and polydisperse monomer distributions. Preliminary results on the coagulation of charged ellipsoidal grains are also presented. The results and implications of these studies are summarized in the following sections.

6.1 Electromagnetic Interactions

Results from coagulation simulated by *Aggregate Builder* suggest that populations assembled from charged-magnetic grains exhibit behavior intermediate to that shown by aggregates assembled from purely charged or magnetic grains, which was the expected behavior. This behavior is clearly seen from examination of both the collision probabilities, Figures 4.2-4.3, and the fractal dimension, characterizing the structure of the result aggregates, Figures 4.4-4.6.

The collision probability for populations grown from charged and charged-magnetic grains leads to the conclusion that the charge on the grain is the primary driver behind the coagulation behavior of aggregates, especially for small N. The magnetization of the grains, however, does provide an additional attractive force between aggregates which enhances the coagulation probability. This difference is

most pronounced for speeds just above the minimum collisional velocity (the speed required to overcome Coulomb repulsion) and small impact parameters. Magnetic forces are seen to play an increasing important role as aggregates grow to larger size, due to the growth of the magnetic dipole moment with N.

When coagulation was simulated using the *box_tree* code, the some different results were observed. Examination of the rate of coagulation of aggregates within the simulated volume show that ballistic grains experience the least frequent collisions, as expected for grains without long-range force interactions. In contrast to the pair-wise simulations, the aggregates which experienced the most frequent collisions were those which were only charged, lacking a magnetization. As the simulation evolves the charged population appears to experience runaway growth of the largest aggregates in the population. Magnetic grains, in contrast, exhibit an enhanced growth rate, compared to ballistic grains, but without runaway growth. Interestingly, the charged-magnetic population appears to grow in a manner most similar to the magnetic population, though with a growth rate slightly enhanced at later simulation times. This is likely due to the lower rebound velocities from failed collisions due to the additional attractive force.

Similar to the results from the pair-wise interactions modeled using *Aggregate Builder*, the magnetic dipole moment is seen to grow steadily in the N-body model as aggregates acquire material through collisions, Figure 4.X. As these different simulations agree, it is reasonable to conclude that the magnetic dipole plays an enhanced role in driving collisions for aggregates of larger size. Aggregates built from magnetic material are seen to have smaller compactness factors, indicating more open and fluffy structures, as seen in Figure 4.X.

The inclusion of both electrostatic and magnetostatic forces during coagulation will grow aggregates which are, structurally, intermediate to the morphologies seen from including either interaction on its own. The rate of growth of aggregates in

astrophysical environments will also be enhanced compared to ballistic or magnetic populations but without the rapid run away growth seen for charged populations. These results not only have significant implications for the early stages of planetesimal formation, which depends upon local conditions within a PPD, but also for coagulation in a laboratory environment, where the structure and size of aggregates may be tuned and selected by the appropriate use of material properties and plasma characteristics.

6.2 Non-Spherical Monomers

Aggregates were grown using a combination of particle-cluster and cluster-cluster aggregation methods for three different monomer shapes: spheres, prolate ellipsoids with aspect ratios of $3:1:1$, $5:1:1$ and $10:1:1$, and oblate ellipsoids with aspect ratios of $3:3:1$, $5:5:1$, and $10:10:1$. Aggregates were assembled using both monodisperse populations as well as polydisperse populations obeying a size distribution given by Equation 5.1, using two different size distributions defined by $\alpha = 1.8$ and $\alpha = 3.5$. The structure of the resulting aggregates were compared according to aggregates radius, compactness factor and friction time.

Deviation from the standard assumption of spherical monomers for modeling dust coagulation has been shown to have a definitive impact on the overall aggregate structure (characterized by the compactness factor) and the relative velocities (characterized by the friction time) for aggregates in astrophysical environments. It has been shown that ellipsoidal monomers form aggregates which are more compact (less fluffy), have a smaller equivalent radii, and exhibit a wider range of responses to turbulent eddies than do aggregates grown from sphericl monomers.

Even so, the wide variation in structure and friction times seen for aggregates of a given size built from ellipsoids may make coagulation more efficient, as large aggregates can still have relatively large differences in relative velocities with each

other, which drives collisions. Large aggregates built from spheres tend to have similar friction times, which leads to small relative velocities, eventually halting aggregate growth.

Numerical models have also been used to charge ellipsoidal monomers and compared to the charges seen for spherical monomers subjected to the same plasma conditions. Ellipsoidal monomers are seen to gain a charge with a greater magnitude, due to the difference in surface area, with the bulk of charges being concentrated at the high curvature ends. This concentration of charges at opposing ends of an ellipsoid also leads to a small dipole moment for single grains.

Clusters of ellipsoids coagulated under the influence of electrostatic interactions exhibit a gradual distribution of charges over an aggregate's surface. The largest monomer charges are seen to exist preferentially on the most exterior monomers with a gradual decrease in charge on monomers closer to the COM. Aggregates grown from spheres show the same arrangement of charges on the most exterior monomers but the interior particles have very little charge. Aggregates built from ellipsoids also grow clusters which are much more compact than those grown using spheres, exhibited by the compactness factor.

6.3 Future Work

Evolution of populations of dust grains, such as in PPD's, are usually studied by employing a statistical approach, where the detailed microphysics of collisions are not included. The Smoluchowski equation is a commonly used method to determing the evolution of the size distribution [5]. The collision microphysics are encapsulated in the coagulation kernel given by

$$Q(y_i, y_i') = A_{coll}(y_i, y_i') v_{rel}(y_i, y_i') S(y_i, y_i') \tag{6.1}$$

where A_{coll} denotes the collisional cross-section, v_{rel} is the relative velocities between

particles, S is the sticking efficiency, and these functions depend on the independent aggregate parameters y_i.

The Smoluchowski equation may be integrated numerically to determine the evolution of a large population of dust for any relevant astrophysical environment if the coagulation kernel may be defined. The definition of this kernel may be done by utilizing the results of coagulation from the numerical methods described in this thesis. The results of this integration may then be compared to current theory and observations of PPD's to determine the most likely combination of dust and plasma parameters present.

The broad range of relative velocities that non-spherical monomers and the aggregates they create may achieve also raise the question of whether all collisions which occur will result in simple sticking. Velocities which are too high can lead to non-sticking results such as bouncing, restructuring (rolling, twisting, sliding) or even destruction of an aggregate by fragmentation. Generally the velocities for which these effects must be considered are not possible for thermal motion. However, at the high curvature ends of ellipsoidal shapes, the energy threshold for inducing restructuring or fragmentation is reduced compared to restructuring energy threshold for spheres of equal volume. It would therefore be of great benefit to examine the possible collisional results and microphysics of non-sticking collisions for non-spherical particles.

Study of the possible effects of non-spherical particles should be continued to fully replicate the studies of Chapter 4 by determination of magnetic dipole moments on ellipsoidal shapes and modeling the resulting coagulation. These interactions may also be employed as a proof of concept for growing a new generation of magnets by deposition of nanometer sized magnetic material, one of strong magnetization, the other of hard, stable magnetization.

BIBLIOGRAPHY

[1] K.C. Smyth and J.H. Miller. Chemistry of Molecular Growth Processes in Flames. *Science*, 236:1540-1546, 1987.

[2] B. Beke. The Process of Fine Grinding. *The Hauge: Nyhoff*, 1:150, 1981.

[3] L.G. Austin, R.R. Kimpel and P.T. Lockie. Process Engineering of Size Reduction in Ball Milling. *Am. Inst. of Mining, Metallurgical and Per. Engineers*, 1984.

[4] W.H. Marlow. Derivation of Aerosol Collision rates for Singular Attractive Contact Potentials. *J. Chem. Phys.*, 73, 1980.

[5] V. Ossenkopf. Dust Coagulation in Dense Molecular Clouds: The Formation of Fluffy Aggregates. *A&A*, 280:617-646, 1993.

[6] G. Suttner, H.W. Yorke and D.N.C. Lin. Dust Coagulation in Infalling Protostellar Envelopes. I. Compact grains. *ApJ*, 524:857, 1999.

[7] J. Blum and G. Wurm. The Growth Mechanisms of Macroscopic Bodies in Protoplanetary Disks. *Ann. Rev. Astron. Astrophys*, 46(1):21-56, 2008.

[8] C.P. Dullemond, F. Brauer and Th. Henning. Coagulation, Fragmentation and Radial Motion of Solid Particles in Protoplanetary Disks. *Astron. Astrophys.*, 2007.

[9] G. Wurm et al. Experiements on the PhotoPhoretic Motion of Chondrules and Dust Aggregates - Indications for the Transport of Matter in Protoplanetary Disks. *Icarus*, 208(1):482-491, 2010.

[10] A. Dutrey, V. Pietu and S. Guilloteau. Probing the Structure of Protoplanetary Disks: A Comparative Study of DM Tau, LkCa 15 and MWC 480. *Astron. Astrophys.*, 2007.

[11] M.C. Wyatt, W.R.F. Dent and J.S.Greaves. SCUBA Observations of Dust Around Lindroos Stars: Evidence for a Substantial Submillimetre Disk Population, *MNRAS*, 342:876-888, 2003.

[12] T. Montmerle et al., Solar System Formation and Early Evolution: The First 100 million Years. *Earth Moon Planets*, 98:39, 2006.

[13] C.P. Dullemond and J.D. Monnier. The Inner Regions of Protoplanetary Disks. *Annu. Rev. Astron. Astrophys.*, 48:205-39, 2010.

[14] S.J. Weidenschilling. Aerodynamics of Solid Bodies in Solar Nebula. *MNRAS*, 180:57-70, 1977.

[15] C. Dominik and H. Nubold. Magnetic Aggregation: Dynamics and Numerical Modeling. *Icarus*, 157:173-186, 2002.

[16] C. Dominik and A.G.G.M. Tielens. The Physics of Dust Coagulation and the Structure of Dust Aggregates in Space. *Astrophysical Journal*, 480:647, 1997.

[17] S. Kempf, S. Pfalzner and T.K. Henning. N-Particle Simulations of Dust Growth I. Growth Driven by Brownian Motion. *Icarus*, 141:388, 1999.

[18] A. Zsom, Z. Sandor and C.P. Dullemond. The First Stages of Planet Formation in Binary Systems: How Far Can Dust Coagulation Proceed. *Atron. Astrophys.*, 527, 2011.

[19] J. Blum and G. Wurm. Experiments on Sticking, Restructuring, and Fragmentation of Preplanetary Dust Aggregates. *Icarus*, 143:138, 2000.

[20] L. S. Matthews and T. W. Hyde. Effects of the Charge-Dipole Interaction on the Coagulation of Fractal Aggregates. *IEEE*, 2004.

[21] H. Nubold, T. Poppe, M. Rost, C. Dominik and K.H. Glassmeier. Magnetic Aggregation II. Laboratory and Microgravity Experiments. *Icarus*, 165:195-214, 2003.

[22] J.C. Simpson, S. Simons and I.P. Williams. Thermal Coagulation of Charges Grains in Dense Clouds. *Astrophys. Space Sci* 61:65, 1979.

[23] L.S. Matthews, R.L. Hayes, M.S. Freed and T.W. Hyde. Formation of Cosmic Dust Bunnies. *IEEE T. Plasma Sci.*, 35:260, 2007.

[24] U. von Zahn and W. Meyer. Mesopause Temperatures in Polar Summer. *J. Geophys. Res*, 941:14647, 1989.

[25] R. Neuber, P. von der Gathen and U. von Zahn. Altitude and Temperature of the Mesopause at 69 deg. N Latitude in Winter. *J. Geophys. Res*, 931:11093, 1988.

[26] G.E. Thomas. Solar Mesosphere Explorer Measurements of Polar Mesospheric Clouds (Noctilucent Clouds). *J. Atmos. Terr. Phys*, 46:819, 1984.

[27] B.B. Balsley, W.L. Ecklund and D.C. Fritts. VHF Echoes from the High Altitude Mesosphere and Lower Thermosphere- Observations and Interpretations. *J. Atmos. Sci*, 40:2451, 1983.

[28] P. Czechowsky, I.M. Reid and R. Ruester. VHF Radar Measurements of the Aspect Sensitivity of the Summer Polar Mesopause Echoes Over Andenes (69 deg N, 16 deg E), Norway. *Geophys. Res. Lett.*, 15:1259, 1988.

[29] M.C. Kelley, D.T. Farley and J. Roettger. The Effect of Cluster Ions on Anomalous VHF Backscatter from the Summer Polar Mesosphere. *Geophys. Res. Lett.*, 14:1031, 1987.

[30] J. Gumble and G. Witt. Rocket-Borne Photometry of NLC Particle Populations. *Adv. Space Res.* 28(7):1053-1058, 2001.

[31] M.T. DeLand, E.P. Shettle, G.E. Thomas and J.J. Olivero. A Quarter-Century of Satellite Polar Mesospheric Cloud Observations. *J. Atmos. Solar Terr. Phys.* 68(1):9-29, 2006.

[32] P. Gabrielli, C. Barbante, J.M.C. Plane, et al. Meteoric Smoke Fallout Over the Holocene Epoch Revealed by Iridium and Platinum in Greenland Ice. *Lett. to Nature*, 432:1011-1014, 2004.

[33] R.G. Keesee. Nucleation and Particle Formation in the Upper Atmosphere. *J. Geophys. Res.* 94:14683, 1989.

[34] O. Havnes, U. de Angelis, R. Bingham, C.K. Geortz, and G.E. Morfill. On the Role of Dust in the Summer Mesopause. *J. Atmos. Terr. Phys.* 52:637, 1990.

[35] J.M. Greenberg and J.I. Hage. From Interstellar Dust to Comets: A Unification of Observations Constraints. *ApJ*, 361:260-274, 1990.

[36] J.I. Hage and J.M. Greenberg. A Model for the Optical Properties of Porous Grains. *Astrophy. Journal*, 361:251-259, 1990.

[37] J.A. McDonnell, et al. *Proc. Workshop on Analysis of Returned Comet Nucleus Samples*, 1989.

[38] E.P. Mazets, et al. Dust in Comet P/Halley from Vega Observations. *A&A*, 187:699-706, 1987.

[39] E.C. Whipple. Potentials of Surfaces in Space. *Rep. Prog. Phys.*, 44:1197, 1981.

[40] D.A. Mendis and M. Rosenberg. Cosmic Dusty Plasma. *Annu. Rev. Astron. Astrophys.*, 32:419, 1994.

[41] H. Nubold and K.H. Glassmeier. Accretional Remanence of Magnetized Dust in the Solar Nebula. *Icarus*, 144:149-159, 2000.

[42] C. Dominik and H. Nubold. Magnetic Aggregation: Dynamics and Numerical Modeling. *Icarus*, 157:181, 2002.

[43] E.I. Chiang and P. Goldreich. Spectral Energy Distributions of T Tauri Stars with Passive Circumstellar Disks. *Astrophys. Jour.* 490(1):368-377, 1997.

[44] C.W. Ormel, M. Spaans and A.G.G.M. Tielens. Dust Coagulation in Protoplanetary Dusks: Porosity Matters. *AA*, 461:215-232, 206.

[45] J. Blum, et al. Growth and Formations of Planetary Seedlings: Results from a Microgravity Aggregation Experiment. *Phys. Rev. Lett.* 85, 2000.

[46] C.P. Dominik, J. Blum, J.N. Cuzzi and G. Wurm. Protostars and Planets V. *Univ. Arizona Press*, 783, 2007.

[47] G. Baumgarten, J. Fiedler and G. von Cossart. The Size of Noctilucent Cloud Particles Above ALOMAR (69N, 16E): Optical Modeling and Method Description. *Adv. Space Res.*, 40(6):772-784, 2007.

[48] P.J. Armitage. Astrophysics of Planet Formation. *Cambridge University Press*, 2010.

[49] S.J. Weidenschilling. Aerodynamics of Solid Bodies in the Solar Nebula. *MNRAS*, 180:57-70, 1977.

[50] F.L. Whipple. On Certain Aerodynamic Processes for Asteroids and Comets. *From Plasma to Planet, Proc.*, 1972.

[51] K. Kornet, T.F. Stepinski, and M. Rozyczka. Diversity of Planetary Systems from Evolution of Solids in Protoplanetary Disks. *Astron. Astrophys.*, 378:180-191. 2001.

[52] T. Takeuchi and D.N.C. Lin. Radial Flow of Dust Particles in Accretion Disks. *Ap.J*, 581:1344-1355, 2002.

[53] A. Zsom, C.W. Ormel, C. Guttler, J. Blum, and C.P. Dullemond. The Outcome of Protoplanetary Dust Growth: Pebbles, Boulders, or Planetesimals?: II. Introducing the Bouncing Barrier. *Astron. Astrophys.*, 513, 2010.

[54] N.I. Shakura and R.A. Sunyaev. Black Holes in Binary Systems. Observational Appearance. *Astron. Astrophys.*, 24:337-355, 1973.

[55] S.A. Balbus and J.F. Hawley. A Powerful Local Shear Instability in Weakly Magnetized Disks. I - Linear Analysis. II - Nonlinear Evolution. *Astrophys. Journ.*, 376:214-233, 1991.

[56] C.W. Ormel and J.N. Cuzzi. Closed-form Expressions for Particle Relative Velocities Induced by Turbulence. *Astron. Astrophys.*, 466:413-420, 2007.

[57] J.N. Cuzzi, R.C. Hogan, J.M. Paque and A.R. Dobrovolskis. Size-selective Concentration of Chondrules and Other Small Particles in Protoplanetary Nebule Turbulence. *Astrophys. Journ.*, 546:496-508, 2001

[58] J.G. Laframboise and L.W. Parker. Probe Design for Orbit Limited Current Collection. *Phys. Fluids*, 16:629, 1973.

[59] V.E. Fortov, A.G. Khrapak, S.A. Krapak, V.I. Molotkov and O.F. Petrox. Reviews of Topical Problems: Dusty Plasmas. *Phys. Usp*, 47:447, 2004.

[60] J.D. Jackson. Classical Electrodynamics. *Wiley*, 1998.

[61] L. D. Landau and E. M. Lifshitz. Mechanics, 3^{rd} Edition. *Butterworth-Heinemann* 1976.

[62] D.C. Richardson. A New Tree Code Method for Simulation of Planetesimal Dynamics. *MNRAS*, 261:396-414, 1993.

[63] D.C. Richardson. Tree Code Simulations of Planetary Rings. *MNRAS*, 269:493-511, 1994.

[64] D.C. Richardson. A Self-Consistent Numerical Treatment of Fractal Aggregate Dynamics. *Icarus*, 115:320-335, 1995.

[65] J. Wisdom and S. Tremaine. Local Simulations of Planetary Rings. *Astron. Jour.* 95:925-940, 1988.

[66] J. Barnes and P. Hut. A Hierarchical O(N log N) Force-Calculation Algorithm. *Nature*, 324:446-449, 1986.

[67] A. Chokshi, A.G.G.M. Tielens, and D. Hollenbach. Dust Coagulation. *Aph.J.*, 407:806-819, 1993.

[68] W. Jones. Theoretical and Observational Determinations of the Ionization Coefficient of Meteors. *Astron. Astrophys.*, 288(4):995-1003, 1997.

[69] L.S. Matthews, R.L. Hayes, M.S. Freed and T.W. Hyde. Formation of Cosmic Dust Bunnies. *IEEE Trans. Plasma Sci.*, 35:260-265, 2007.

[70] Q. Ma, L.S. Matthews, V. Land and T. W. Hyde. Charging of Interstellar Dust Grains Near the Heliopause. *arXiv* 2011.

[71] Q. Ma, Charging of Aggregate Grains in Astrophysical Environments. *Baylor University*, 2012.

[72] S. Auer, S. Kempf and E. Grun. Computed Electric Charges of Grains with Highly Irregular Shapes. on Dust in Planetary Systems, 177-180, 2007.

[73] L.S. Matthews and T.W. Hyde. Charging and Growth of Fractal Dust Grains. *IEEE Trans. on Plasma Sci.*, 36(1), 2008.

[74] D. Paszun and C. Dominik. Collisional Evolution of Dust Aggregates. From Compaction to Catastrohpic Destruction. *Astron. Astrophys.*, 507:1023, 2009.

[75] R. W. Saunders and J. M. C. Plane. A Laboratory Study of Meteor Smoke Analogues: Composition Optical Properties and Growth Kinetics. *Journ. Atmo. and Solar Terr. Phys.*, 68:2181-2202, 2006.

[76] E. Anders. Origin, Age and Composition of Meteorites. *Sp. Sci. Reviews* 3:583-714, 1964.

[77] L. S. Matthews and T. W. Hyde. Effects of the Charge-Dipole Interaction on the Coagulation of Fractal Aggregates. *IEEE Trans. Plasma Sci.* 32(2):586-593, 2004.

[78] I Bertinit, P. J. Gutierrez and W. Sabolo. The Influence of the Monomer Shape in the First Stage of Dust Growth in the Protoplanetary Disk. *A&A*, 504:625-633, 2009.

[79] D. Paszun and C. Dominik. The Influence of Grain Rotation on the Structure of Dust Aggregates. *Icarus* 182:274-280, 2006.

[80] C. W. Ormel et al. Dust Coagulation and Fragmentation in Molecular Clouds II. The Opacity of the Dust Aggregate Size Distrbution. *A&A* 532, 2011.

[81] J. S. Mathis, W. Rumpl and K. H. Nordsieck. The Size Distrbution of Interstellar Grains. *Astrophys. Jour.* 217:425-433, 1977.